GAZİ ÜNİVERSİTESİ

1926

# IMPROVING THE SPEED OF DYNAMIC ATOMIC FORCE MICROSCOPE WITH MULTIFREQUENCY APPROACH

A THESIS SUBMITTED TO
THE GRADUATE SCHOOL OF NATURAL AND APPLIED SCIENCES
OF
GAZİ UNIVERSITY

BY

Sena Nur EKİCİ

IN PARTIAL FULFILLMENT OF THE REQUIREMENTS
FOR
THE DEGREE OF MASTER OF SCIENCE
IN
ELECTRICAL AND ELECTRONICS ENGINEERING DEPARTMENT

JULY 2023

## ETHICAL STATEMENT

I hereby declare that in this thesis study I prepared in accordance with thesis writing rules of Gazi University Graduate School of Natural and Applied Sciences;

- All data, information and documents presented in this thesis have been obtained within the scope of academic rules and ethical conduct,
- All information, documents, assessments and results have been presented in accordance with scientific ethical conduct and moral rules,
- All material used in this thesis that are not original to this work have been fully cited and referenced,
- No change has been made in the data used,
- The work presented in this thesis is original,

or else, I admit all loss of rights to be incurred against me.

Sena Nur EKİCİ
20/07/2023

# IMPROVING THE SPEED OF DYNAMIC ATOMIC FORCE MICROSCOPE WITH MULTIFREQUENCY APPROACH

(M. Sc. Thesis)

Sena Nur EKİCİ

GAZİ UNIVERSITY

GRADUATE SCHOOL OF NATURAL AND APPLIED SCIENCES

July 2023

## ABSTRACT

In this thesis, the state-of-the-art high-speed dynamic atomic force microscope (HS-AFM) with *a* *Q*-controlled cantilever is simulated with different control approaches in MATLAB/Simulink. This study assesses the performance of the controllers which are the conventional PI controller, and the robust $H_\infty$ controller in both air and liquid environments by using a small high-frequency cantilever. In addition, the control technique named $H_\infty$+ P, which combines proportional and $H_\infty$ control, is implemented specifically for an air environment. The performance of controllers is analyzed in terms of scan speed and accuracy under noise, disturbance, and uncertainty for the same topography. The simulation results show that the PI and $H_\infty$ controllers exhibit similar responses in a liquid environment. On the other hand, in terms of overall performance under exogenous effects in air, the $H_\infty$+P controller responds better than the PI and $H_\infty$ controllers. Furthermore, the HS-AFM system proposed in this study can achieve scan rates that are about 6 times in liquid faster than the current state-of-the-art HS-AFM systems.

| | | |
|---|---|---|
| Science Code | : | 90529 |
| Key Words | : | High-speed dynamic AFM, Tapping mode, PI control, Robust $H_\infty$ control, *Q*-control, Exogenous effects, Noise, Disturbance, Uncertainty |
| Page Number | : | 55 |
| Supervisor | : | Assoc. Prof. Dr. Müjdat BALANTEKİN |

ÇOKLU-FREKANS YAKLAŞIMI İLE DİNAMİK ATOMİK KUVVET MİKROSKOBU HIZININ İYİLEŞTİRİLMESİ

(Yüksek Lisans Tezi)

Sena Nur EKİCİ

GAZİ ÜNİVERSİTESİ

FEN BİLİMLERİ ENSTİTÜSÜ

Temmuz 2023

ÖZET

Bu tezde, *Q*-kontrollü proplu en son teknoloji yüksek hızlı dinamik atomik kuvvet mikroskobu (YH-AKM), farklı kontrol yaklaşımlarıyla MATLAB/Simulink'te simüle edilmiştir. Bu çalışmada, küçük yüksek frekanslı prop kullanarak geleneksel PI kontrolcü, gürbüz $H_\infty$ kontrolcüsünün performansları hem hava hem de sıvı ortamlarda değerlendirilmiştir. Ayrıca, yalnızca hava ortamında kullanılan oransal ve $H_\infty$ kontrolünün birleşimi olan $H_\infty$+ P önerilmiştir. Kontrolcülerin performansı, aynı topografi kullanarak gürültü, bozukluk ve belirsizlik koşullarında tarama hızı ve doğruluğu açısından analiz edilmiştir. Simülasyon sonuçları, PI ve $H_\infty$ kontrolcülerinin sıvı ortamında benzer tepkiler verdiğini göstermektedir. Öte yandan, hava ortamındaki dış etkilere karşı genel performans açısından, $H_\infty$+P kontrolcüsü, PI ve $H_\infty$ kontrolcülerinden daha iyi bir yanıt vermektedir. Dahası, bu çalışmada sunulan YH-AKM sistemi, mevcut en son teknoloji YH-AKM sistemlerine göre sıvıda yaklaşık 6 kat daha hızlı tarama hızlarına ulaşabilmektedir.



| | | |
|---|---|---|
| Bilim Kodu | : | 90529 |
| Anahtar Kelimeler | : | Yüksek hızlı dinamik AFM, Hafif vurma modu, PI kontrolü, Gürbüz $H_\infty$ kontrolü, *Q*-Kontrol, Dışsal etkiler, Gürültü, Bozukluk, Belirsizlik |
| Sayfa Adedi | : | 55 |
| Danışman | : | Doç. Dr. Müjdat BALANTEKİN |

## ACKNOWLEGMENT

Firstly, I would like to extend my sincere appreciation to my advisor, Assoc. Prof. Dr. Müjdat BALANTEKİN, for his invaluable understanding, guidance, encouragement, and unwavering support throughout every phase of my thesis research.

I would like to express my gratitude for the financial support provided by TÜBİTAK's 2210-A General Domestic Master's Scholarship Program.

I extend my gratitude to the committee members, Assoc. Prof. Dr. Tuğba SELCEN NAVRUZ and Prof. Dr. Hüseyin CANBOLAT, for their valuable contributions that greatly assisted me in revising the thesis.

Finally, I would like to thank my parents, and my brother for their unconditional and endless support.

# TABLE OF CONTENTS

**Page**

# LIST OF TABLES

**Table** **Page**

## LIST OF FIGURES

**Figure** **Page**

# LIST OF ABBREVIATIONS AND SYMBOLS

In this study, the symbols and abbreviations used are presented below, along with their explanations.

| Symbols | Explanations |
|---|---|
| **GPa** | Giga-Pascal |
| **dB** | Decibel |
| **Mhz** | MegaHertz |
| **N/m** | Newton per meter |
| **rad/s** | Radian per second |
| **krad/s** | Kiloradian per second |
| **µs** | Microseconds |
| **ms** | Miliseconds |
| ° | Degree |
| **nm** | Nanometer |
| **Δf** | Frequency shift |

| Abbreviations | Explanations |
|---|---|
| **AC** | Alternating Current |
| **AFM** | Atomic Force Microscope |
| **AM-AFM** | Amplitude Modulation Atomic Force Microscope |
| **DC** | Direct Current |
| **DMT** | Darjaguin Miller Toparov |
| **DNA** | Deoxyribo Nucleic Acid |
| **EM** | Electron Microscope |
| **FM** | Frequency Modulation Atomic Force Microscope |
| **FGPA** | Field Programmable Gate Array |
| **FPS** | Frame per Second |
| **Hinf** | H infinity |
| **Hinf+P** | H infinity+Proportional |
| **HS-AFM** | High Speed Atomic Force Microscope |

| Abbreviations | Explanations |
|---|---|
| **MF-AFM** | Multifrequency Atomic Force Microscope |
| **NA** | Non-Applicant |
| **NC-AFM** | Non-contact Atomic Force Microscope |
| **OBD** | Optical Beam Deflection |
| **PI** | Proportional- Integral |
| **PLL** | Phase Locked Loop |
| **Q-factor** | Quality factor |
| **RMS** | Root Mean Square |
| **RNA** | Ribo Nucleic Acid |
| **SEM** | Scanning Electron Microscope |
| **SPM** | Scanning Probe Microscope |
| **STM** | Scanning Tunneling Microscope |
| **VGA** | Variable Gain Amplifier |

# 1. INTRODUCTION

In modern times, a variety of microscopy techniques have been developed to meet the specific needs of different applications. Optical microscopes are capable of working on a micrometer scale. The advent of nanotechnology has led to the development of instruments such as Scanning Probe Microscopes (SPM) and Electron Microscopes (EM), which allow for the investigation of samples on a nanometer scale. In order for an electron microscope to produce images, the surface of the sample must be conductive to reflect the electron beams and allow for measurement of their properties. However, this requirement for a conductive surface makes it challenging to observe biological samples, and the dynamic processes within them cannot be easily observed using this technique [1].

Scanning Probe Microscope (SPM) has two main types of techniques which are Scanning Tunneling Microscope (STM) and Atomic Force Microscope (AFM) [2]. These methods utilize a probe to scan the surface of a sample and create high-resolution images that reveal the sample's topography and properties at the nanometer scale. STM involves tracking the surface of conductive samples using a sharp metal tip. An electric voltage is applied between the tip and the surface of the conductive sample, causing electrons to tunnel through the small gap between the two. As a result of this process, a measurable electrical current is generated. By monitoring and measuring this current, STM can create a highly detailed image of the sample's topography and electronic structure at the atomic scale.

AFM is an indispensable tool for imaging various kinds of samples at the nanometer scale. It allows for the visualization of sample topography, characterization of mechanical properties and surface chemistry of materials, as well as manipulation of nanoscale materials. There are various types of samples that can be used in AFM, including biological samples such as DNA/RNA [3-5], proteins [6], membranes [7], and chemical materials such as polymers, metals, and semiconductors. Therefore, AFM has become increasingly popular in microbiology, materials science, and many other nano-scientific research fields. The main advantage of AFM is its ability to operate in multiple environments such as vacuum, air, and liquid. Additionally, unlike STM, it can operate on non-conductive samples.

High-speed AFM (HS-AFM) [6, 8-9] achieves a faster imaging rate compared to conventional AFM by using fast-scanning probes and advanced control electronics.

This enhanced imaging performance enables the visualization of the dynamic behavior of biomolecules and real-time examination of samples, such as the study of Ando and coworkers' video imaging of myosin V [10]. As a result, HS-AFM has become the primary tool for a wide range of applications.

In this thesis, the objective is to improve the HS-AFM system imaging rate and robustness. The main factor that limits the imaging rate is the *z*-piezo because of its limited bandwidth. To overcome this limitation, a technique called bimodal multifrequency AFM [11-14] is employed. In this approach, the fundamental eigenmode amplitude is utilized as the actuator instead of using a *z*-piezo, while higher eigenmode oscillation is used for the feedback. By exciting the cantilever with both the first and higher eigenmode resonance frequencies simultaneously, the capabilities of the system are expanded. Another limitation of the imaging rate is the high *Q*-factor, especially in the air. Therefore, the *Q*-factor is reduced artificially by using the *Q*-Control method [15-19], which is basically adding cascade phase shifter and gain to fundamental eigenmode oscillation [20-21].

In addition, different controller approaches are applied to the proposed system. One of them is the PI controller, which is a commonly used controller method in conventional AFM systems [22-23]. Another approach is the $H_\infty$ controller, which is employed in research to enhance imaging rate and system robustness [24-28]. Furthermore, the combination of the PI and $H_\infty$ controllers, named the $H_\infty$+P controller, is proposed specifically for the air environment. The performances of all controllers in this enhanced HS-AFM system are compared in terms of robustness to exogenous effects and system speed.

In Chapter 2, an overview of the AFM, introducing its general structure, working principle, and operation modes are provided. Additionally, a brief introduction to HS-AFM and its applications are explained.

In Chapter 3, the concept of multifrequency AFM and its significance is explained. The state-of-the-art HS-AFM system with a *Q*-controlled cantilever is introduced, along with a proposed block diagram detailing the *Q*-controlled cantilever's functionality. The process behind the block diagram is thoroughly explained, including the system parameters employed for simulations and their respective roles.

In Chapter 4, the importance of implementing a feedback control loop in an AFM system is explained. Different types of feedback control loops suitable for AFM systems are discussed, with a particular focus on the theory behind PI, $H_\infty$, and the combined controller named $H_\infty$ + P. Each controller's functionality and operation are detailed in this chapter.

# 2. GENERAL STRUCTURE OF AFM

Figure 2.1 illustrates the working principle of an AFM. In AFM, a cantilever equipped with a sharp tip is employed to scan the surface of a sample. The interaction forces between the tip and the sample cause the cantilever to deflect. To measure this deflection, the Optical Beam Deflection (OBD) technique [29] is used because of its simplicity. With this method, the displacement of the cantilever tip can be measured by detecting the laser beam reflected from the cantilever onto a photodiode sensor. The angle of the laser beam that is reflected onto the photodiode is proportional to the deflection of the cantilever.

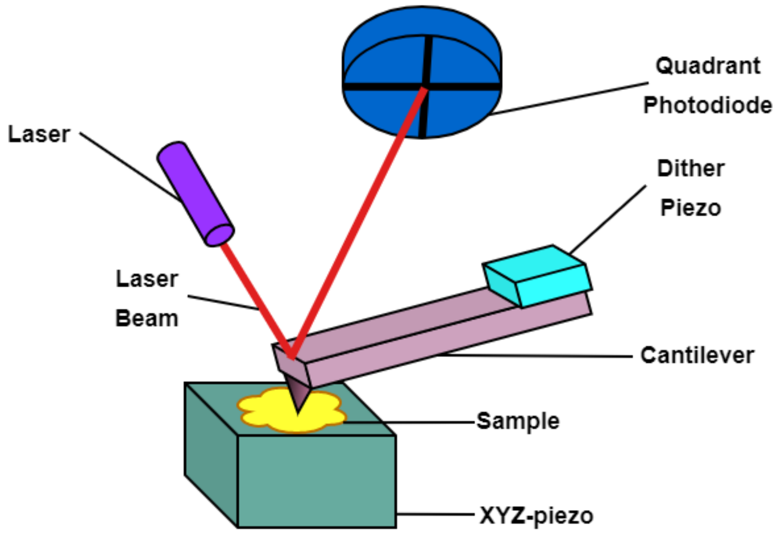


Figure 2.1. Basic AFM principle

To comprehend the functioning mechanism of the entire system, it is essential to have a clear understanding of each of its individual components. The dither piezo is a piezoelectric element that is used to vibrate the cantilever at its resonance frequency. A quadrant photodiode is a type of photodetector commonly used in AFM systems to detect the deflection of the cantilever. The cantilever and *XYZ*-scanner are explained in subsections 2.2 and 2.3 in detail.

## 2.1. High Speed Atomic Force Microscope

A high speed atomic force microscope (HS-AFM) is an advanced imaging tool that allows for the visualization of samples at the nanoscale with high resolution.

High speed AFMs have been developed to minimize the required time per frame, enabling real-time observation of dynamic processes occurring at the nanoscale. HS-AFMs can achieve high imaging speeds by using various techniques such as faster scanning methods [30-32], advanced feedback control algorithms [33-36], using small cantilever [5, 30, 37-40] and actuator. These advancements allow for real-time video imaging of biological samples in action. Figure 2.2 shows a dynamic view of a biological sample, Myosin V.

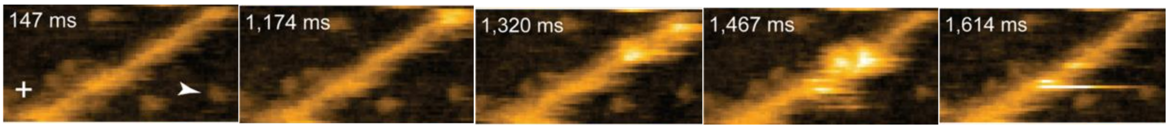


Figure 2.2. “Myosin V (M5-HMM) movement on actin filament captured by HS-AFM” [10]

## 2.2. Cantilevers

Silicon nitride is used to fabricate the cantilever, which has a sharp tip. Typically, the cantilever has a rectangular shape with a conical or pyramidal tip, though its size and shape can vary depending on the intended application. Figure 2.3 shows a commonly used type of AFM cantilever.

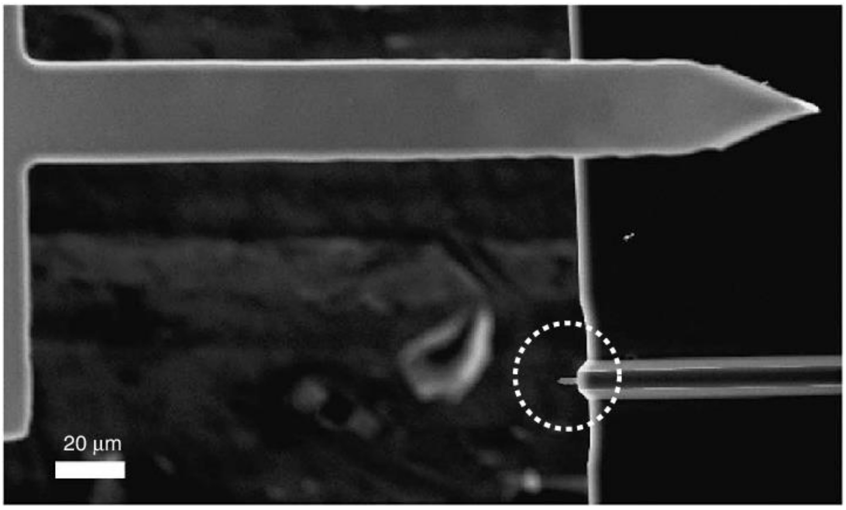


Figure 2.3. “SEM micrograph of a conventional AFM cantilever (Olympus OMCL-AC240TS) and a small cantilever (Olympus BL-AC10DS; encircled)” [41]

Figure 2.4 shows that the cantilever beam can be represented by an equivalent single mode point mass cantilever model [42]. $L$ represents the cantilever length, $m$ is the cantilever mass, and $k$ is the spring constant which refers to the stiffness of the cantilever.

$\zeta$ is the damping ratio, and $x$ represents the tip displacement that occurs in response to a force $F_{drive}$ applied to the cantilever. These three parameters are very important and effect the sensitivity, resonance frequency, and force measurements in an AFM system.

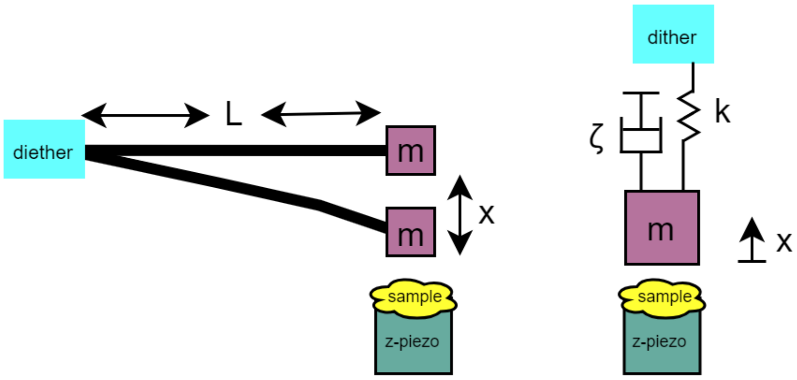


Figure 2.4. Cantilever point-mass model

The length of the cantilever is directly proportional to its resonance frequency, meaning that longer cantilevers have higher resonance frequencies and limited scan speeds. Additionally, the displacement of the cantilever is also affected by its length.

A heavier cantilever exhibits lower sensitivity to sample features and a lower resonance frequency. The force applied to the sample is proportional to the mass of the cantilever.

The force required to excite the cantilever, which is described later in the System Model (3.4) section, is inversely proportional to the spring constant. A stiffer cantilever requires more force to be deflected than a softer cantilever, resulting in reduced sensitivity for stiffer cantilevers. Therefore, softer cantilevers are more sensitive to surface features. On the other hand, stiffer cantilevers have higher resonance frequencies than softer ones, and this affects the imaging rate of the system.

The damping ratio affects the cantilever's resonance behavior as shown in Figure 2.5. In an underdamped system, the damping ratio is less than 1.

In this case, the resonance peak is relatively sharp and has a higher amplitude. The energy of the vibrating cantilever is slowly dissipated over time, causing a slow response. In a critically damped system, the damping ratio is 1 ($\zeta$ = 1). This results in a faster response without any overshoot as illustrated in Figure 2.6. The resonance peak is broad and has the least amplitude.

The system quickly returns to its equilibrium position. In an overdamped system, the damping ratio is greater than 1 ($\zeta > 1$). A higher damping ratio will result in a broader resonance peak with a lower amplitude.

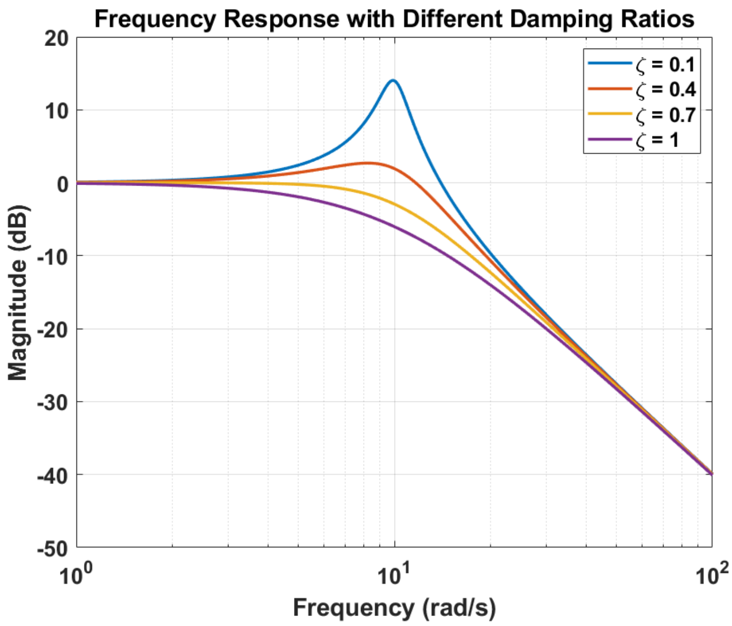


Figure 2.5. Frequency response plot for a system with varying damping ratios

The damping ratio also affects the stability of the AFM system. If the damping ratio is too low, the cantilever will exhibit large amplitude oscillations, which can lead to instability in the system. On the other hand, if the damping ratio is too high, the cantilever will be overdamped, resulting in faster response and reduced sensitivity. Overall, choosing the values of $L, m, k,$ and $\zeta$ for the cantilever is critical, and a trade-off must be made based on the specific application requirements. The mathematical representation of the cantilever according to the point mass model which is a second-order differential equation is expressed as follow

$$m\ddot{x} + \zeta\dot{x} + kx = F_{drive} + F_{ts}(z) \tag{2.1}$$

$F_{drive}$ is applied through dither piezo, and $F_{ts}$ is the tip-sample interaction force that is dependent on the tip-sample distance *z*.

The *i*'th eigenmode natural frequency $\omega_i$ and the damping ratio are known as equations 2.2 and 2.3, respectively. Here, *i* is an integer number ranging from 1 to 3.

$$\omega_i = \sqrt{\frac{k_i}{m_i}} \tag{2.2}$$

$$\zeta_i = \frac{\omega_i m_i}{Q_i} \tag{2.3}$$

$k_i$ and $Q_i$ are the spring constant and the quality factor of *i*'th eigenmode cantilever oscillation, respectively. Substituting equations 2.2 and 2.3 into equation 2.1 yields as follows

$$\frac{k_i}{\omega_i^2}\ddot{x}_i + \frac{k_i}{\omega_i Q_i}\dot{x}_i + k_i x_i = F_{drive} + F_{ts}(z) \tag{2.4}$$

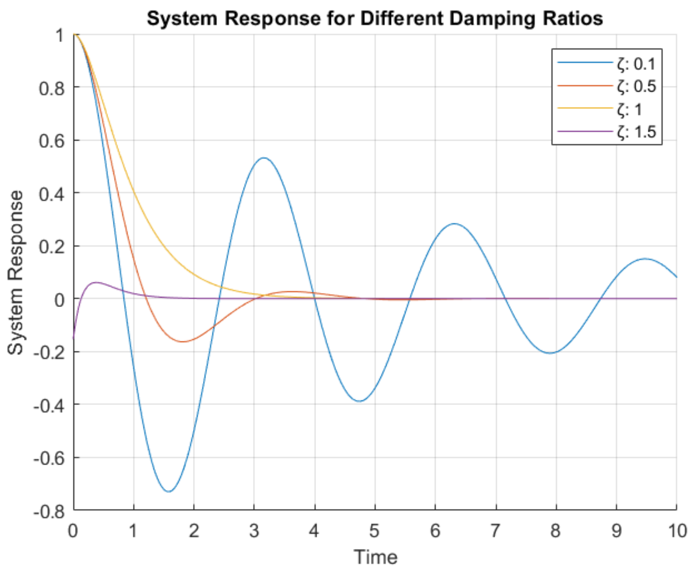


Figure 2.6. Variation of AFM system response with damping ratios

## 2.3. *XYZ*- Scanner

An *XYZ*-scanner is used for three-dimensional imaging and measurements in AFM. A piezoelectric tube actuator bends due to the voltage difference. Voltage difference adjusted by the feedback leads to the bending of the piezoelectric tube actuator in the *X*- or *Y*- directions.

This movement in *X*- or *Y*- directions allow for to lengthen of the piezo along the Z- direction as shown in Figure 2.7 [43].

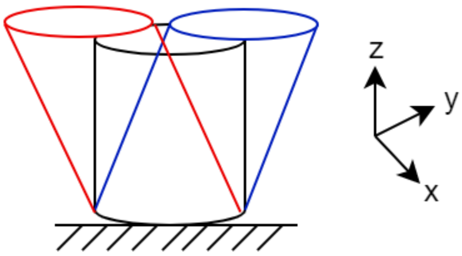


Figure 2.7. Operational principle of piezo tubes

## 2.4. Operation Modes

AFM had three major operation modes, which are tapping mode, non-contact mode, and contact mode.

The classification of tapping mode and non-contact mode as dynamic mode AFM is based on their oscillation during the tracking of the sample surface. In contrast, contact mode is categorized as a static mode AFM since it operates by simply touching the sample surface without any oscillation. The illustrations of dynamic and static mode AFM are shown in Figure 2.8 and Figure 2.9, respectively.

Static mode AFM operates by the deflection of the cantilever tip due to interaction forces, which can be mathematically described by Hooke's Law, as shown in below

$$F = kx \tag{2.5}$$

Here, *F* is the interaction force, *k* is the spring constant and *x* is the amount of cantilever deflection.

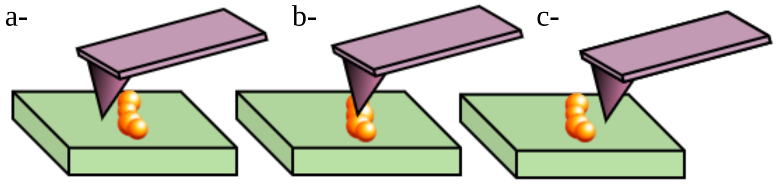


Figure 2.8. The cantilever position in static mode AFM: a) Cantilever tip position before the sample, b) Cantilever tip position during the sample, c) Cantilever tip position after the sample

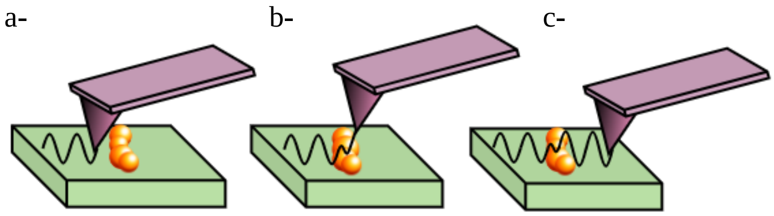


Figure 2.9. The cantilever position in dynamic mode AFM: a) Cantilever tip position before the sample, b) Cantilever tip position during the sample, c) Cantilever tip position after the sample

Static mode AFM has the advantage of being less complex compared to other modes. The basic concept of this mode involves the deflection of the cantilever in response to the upward and downward topographical features of the sample surface. The deflection of the cantilever is detected by a photodiode that measures the displacement of a laser beam directed at the cantilever tip. The DC signal produced by the photodiode is then compared to a set point, and the result is used to adjust the location of the *z*-piezo. In static mode AFM, lateral forces can cause damage to both the cantilever tip and soft samples. Additionally, the feedback speed may be inadequate to keep up with sudden and significant changes in the sample surface, resulting in potential imaging inaccuracies.

In dynamic mode, the cantilever oscillates at or near its resonance frequency and does not touch the sample surface constantly. The cantilever is excited with a sinusoidal wave, which results in a sinusoidal output from the photodiode that includes an amplitude and phase component. Tapping mode AFM involves the cantilever vibrating at or near its resonance frequency with a constant amplitude on the nanometer scale. This intermittent contact allows lateral forces to be minimized, making it the preferred mode for soft samples such as biomolecules, including DNA, RNA, proteins, and cells.

The main drawback of this mode is its slow imaging speed, which is due to the extraction of the sample topography from the output AC signal of the photodiode using amplitude or frequency modulation methods. This extraction process takes more time than the contact mode, making the overall imaging speed slower. The amplitude modulation AFM (AM-AFM) [44-46] is the most preferred technique in tapping mode. This is because AM-AFM is easier to implement and requires less expertise and experience compared to frequency modulation AFM (FM-AFM). The imaging parameters can be set up quickly, and it is easier to optimize the imaging conditions. In this method, the cantilever is excited with the force that is *kA/Q*. A is the given free amplitude. This excitation is done by dither piezo attached to the cantilever.

The photodiode measures the tip oscillation. The amplitude of the tip oscillation is measured using a peak detector. The feedback controller keeps the cantilever oscillation constant at a given set point. The controller output signal provides the sample surface topography. The AM-AFM schematic is given in Figure 2.10. The amplitude of oscillation increases as the sample topography decreases, and similarly, it decreases as the sample topography increases.

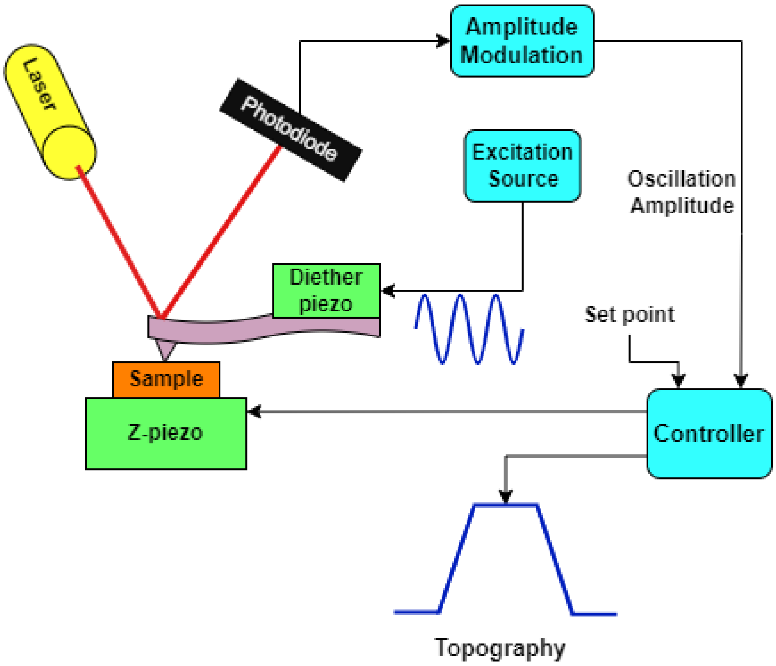


Figure 2.10. AM-AFM schematic

In non-contact AFM (NC-AFM), AFM operates without physical contact between the cantilever and the sample surface.

Instead, it uses a FM-AFM [47] to detect the Van der Waals forces between the tip and the sample surface. This modulation allows for a more sensitive measurement of the Van der Waals forces between the tip and the sample, which can be used to obtain high-resolution images of the sample surface with atomic-scale resolution.

However, NC-AFM typically has a slower imaging speed than contact-mode AFM, due to the need for precise control of the tip-sample distance to keep the non-contact regime. The schematic of FM-AFM is shown in Figure 2.11.The Phase-Locked loop (PLL) is employed for both detecting the frequency shift ($\Delta f$) of the tip oscillation and exciting the cantilever through a dither piezo.

The feedback control is used to regulate the excitation frequency of the cantilever and maintain a constant phase difference between the cantilever excitation and deflection signal. As a feedback control parameter, the frequency shift is used.

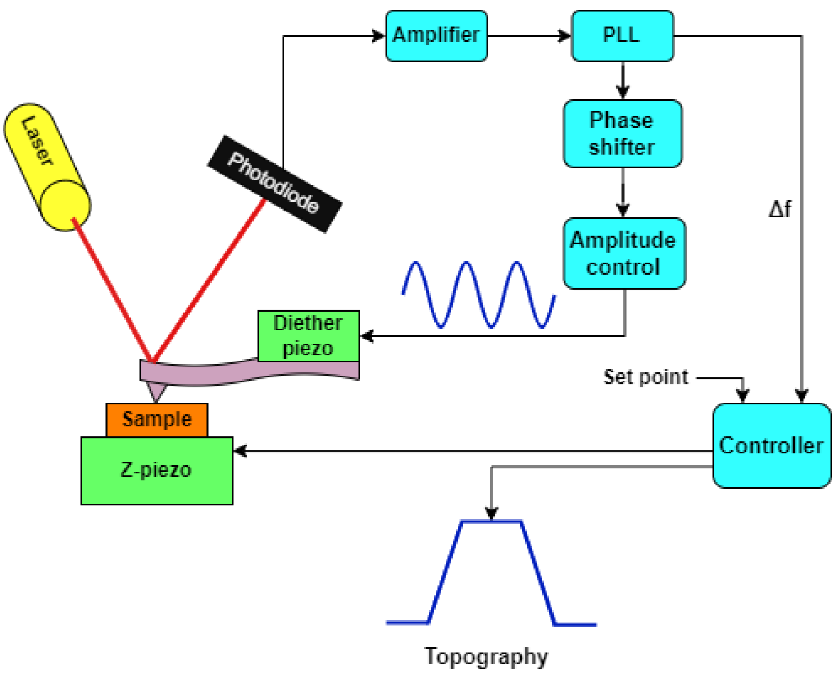


Figure 2.11. FM-AFM schematic

Overall, AM-AFM is preferred in this thesis for imaging soft or delicate samples.

## 2.5. Interaction Forces

In AFM, the interaction forces are measured by detecting the deflection of the cantilever due to the interaction with the sample. There are two major forces which are van der Waals forces and contact forces. Van der Waals forces are attractive and become stronger as the tip gets closer to the sample surface. Contact forces arise when the tip contact with the sample surface.

Contact forces can be repulsive or attractive due to the surface properties and the force applied by the cantilever. Interaction force varies due to the tip-sample distance. The force and tip-sample distance relationship is shown in Figure 2.12 [48].

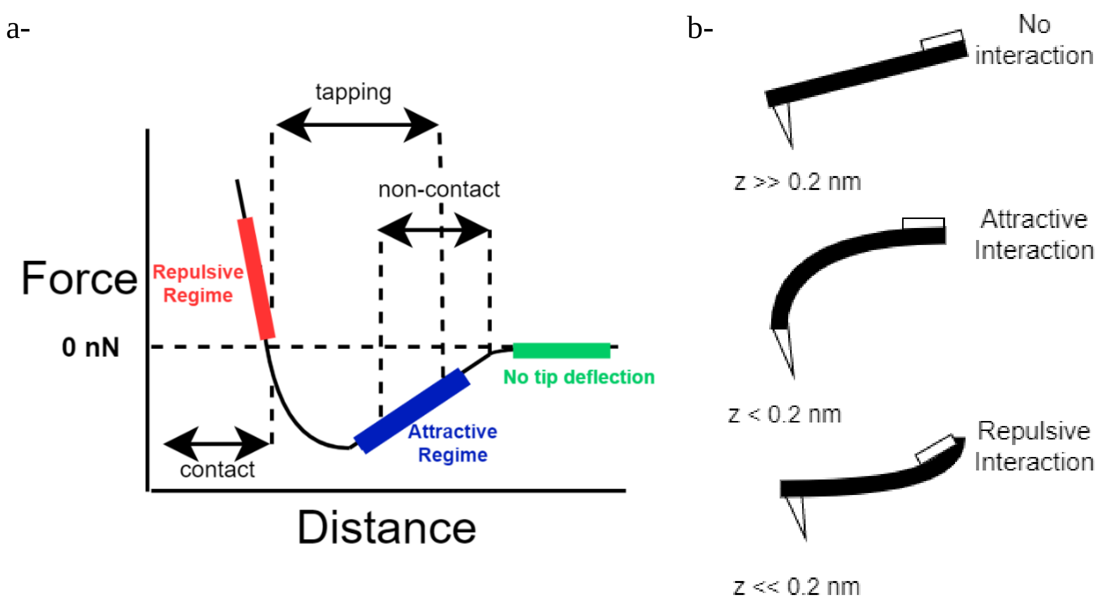


Figure 2.12. a) Regimes of interaction forces as a function of distance, b) Cantilever deflection corresponding to each regime

The attractive van der Waals force affects the tip when the tip-sample distance exceeds the inter-atomic distance. As a result, the tip tends to bend towards the sample surface. At greater distances, the amplitude of the van der Waals force is weak, resulting in higher oscillation amplitude in tapping mode. As the tip approaches the sample surface, the amplitude of the van der Waals force increases. When the tip-sample distance is less than or equal to, the tip experiences a repulsive force and tends to bend away from the sample surface.

The Derjaguin-Miller-Toparov (DMT) model is employed in this study to simulate the interaction forces. For the DMT model, the amplitude of the interaction force is expressed below

$$F_{ts}(z) = \begin{cases} -\dfrac{HR}{6z^2}, & z > a_0 \\ -\dfrac{HR}{6a_0^2} + \dfrac{4}{3}E^*\sqrt{R}(a_0 - z)^{3/2}, & z \leq a_0 \end{cases} \tag{2.6}$$

*H* is the Hamaker constant which describes the strength of the attractive van der Waals forces between the tip of the cantilever and the sample surface, *R* is the tip radius, *d* is the tip-sample distance and *E** is the effective tip-sample elasticity which determines the sensitivity of the AFM system to changes in the sample surface.

# 3. SYSTEM MODEL

## 3.1. Multifrequency AFM

Multifrequency atomic force microscopy (MF-AFM) is a technique used to study the surface topography, properties, and dynamics of materials at the nanoscale by applying several frequencies to the cantilever during scanning [49-50]. The main advantage of MF-AFM is that it allows for the simultaneous measurement of multiple material properties, such as mechanical stiffness, adhesion, and dissipation. This is because the different frequencies used in the technique excite different modes of the cantilever motion, each with a different sensitivity to material properties. When exciting the cantilever at its resonance frequency of two eigenmodes, it is called bimodal AFM, as shown in Figure 3.1.

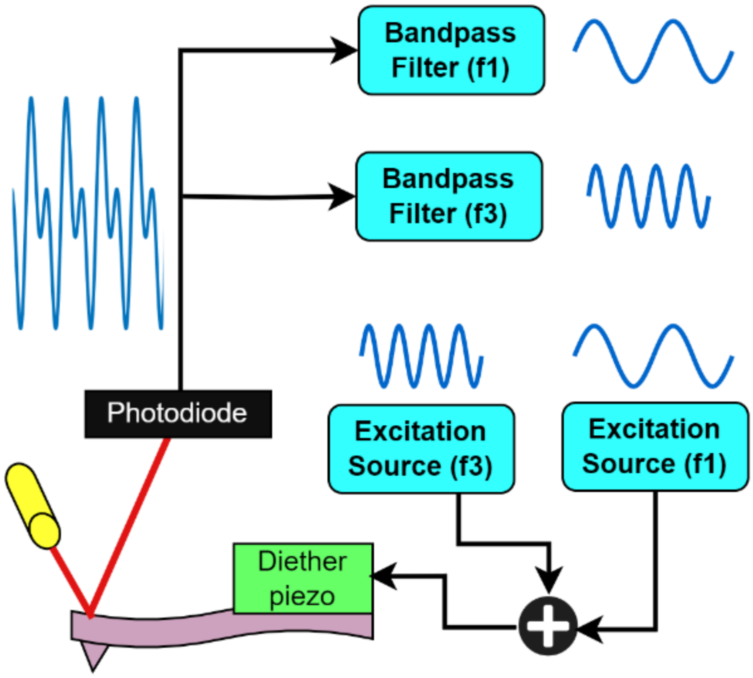


Figure 3.1. Bimodal AFM schematic

In this study, the first eigenmode amplitude is used as the actuator, and the third eigenmode is used for the feedback control loop. Overall, MF-AFM is a powerful technique for studying the nanoscale properties of materials, and it has applications in fields such as materials science, biology, and nanotechnology.

## 3.2. *Q*- Control Method

In tapping mode, one of the limitations of the imaging speed is the transient response of the cantilever. As we mentioned before in cantilever section 2.2, the imaging speed of the cantilever is proportional to the cantilever's resonant frequency, which is mainly determined by the cantilever mass, elastic modulus, and the quality factor *Q*, which depends on the cantilever damping. The *Q*-factor is defined as the ratio of the energy stored in the cantilever's oscillation to the energy lost per cycle due to damping. When the *Q*-factor is low, the transient response of the system will reach a steady state faster. Therefore, to speed up the transient response of the cantilever, a high resonance frequency, and a low *Q*-factor are required [51]. The effect of the *Q*-factor on the cantilever is shown in Figure 3.2.

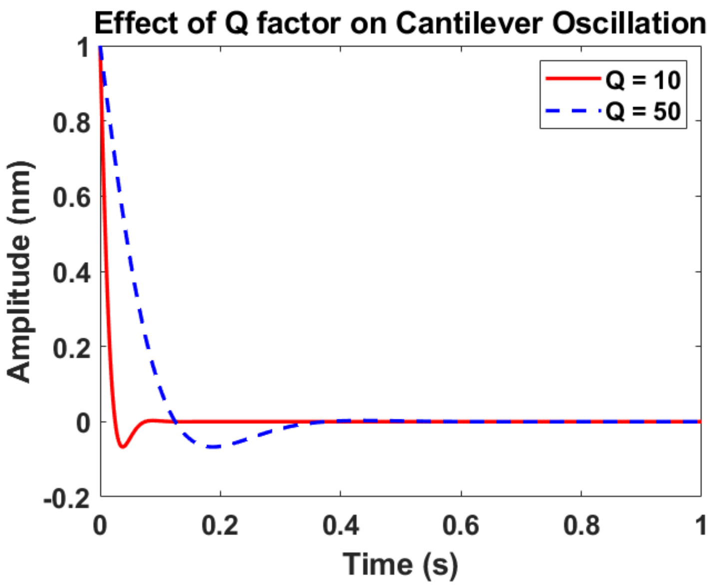


Figure 3.2. Effect of *Q*-factor on cantilever oscillation

The quality factor is 1 for the critically damped system according to equation ($Q$=1/ 2$\zeta$). The quality factor varies depending on the environment. Due to the viscous damping, the *Q*-factor is lower ($Q\approx$ 2-4) in a liquid environment, which means that the imaging speed is higher. In this study, we actively reduce the quality factor by using the *Q*-control method. By using this method, the displacement signal is phase-shifted by 180$^\circ$ and added to the excitation signal that drives the cantilever. The schematic showing the *Q*-control method in tapping mode AFM is shown in Figure 3.3 [52-55].The effective *Q*-factor ($Q_{eff}$) is determined by using equation 3.1 [56].

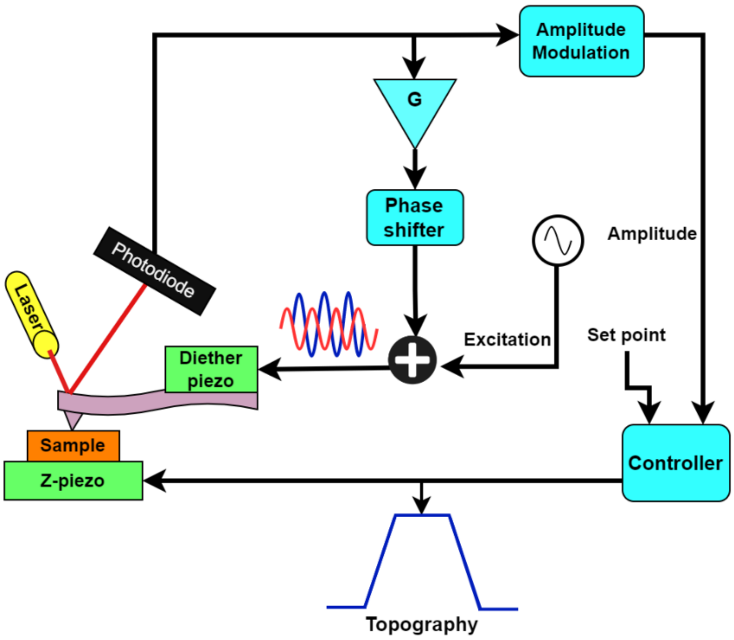


Figure 3.3. AM-AFM with *Q*-control

$$Q_{eff} = \frac{\omega_0 m^*}{\zeta_{eff}} \tag{3.1}$$

$Q_{\text{eff}}$, effective *Q*-factor can be increased or decreased by changing the effective damping ratio $\zeta_{\text{eff}}$ and the effective mass of the cantilever $m^*$ is expressed below

$$\zeta_{eff} = \zeta + \frac{G}{w} \tag{3.2}$$

$$m^* = \frac{k}{\omega_0^2} \tag{3.3}$$

The gain *G* used in *Q*-control is obtained in (3.4) by replacing (2.3), (3.2), and (3.3) in the (3.1) equation. The $Q_{eff}$ value is selected to be as low as possible while ensuring system stability and maintaining $G>0$. The specific values of the selected $Q_{eff}$ are provided in section 3.4.

$$G = k\left(\frac{1}{Q_{eff}} - \frac{1}{Q}\right) \tag{3.4}$$

### 3.3. System Overview

In this study, a state-of-the-art HS-AFM system with *a* *Q*-controlled cantilever is simulated in MATLAB/Simulink environment.

The system is modeled using AM-AFM, with three different signals used to excite the cantilever: first and third eigenmode oscillation, as well as *Q*-controlled first eigenmode oscillation amplitude, as mentioned in the Multifrequency section (3.1).

A DC gain bias is applied to the third eigenmode oscillation to prevent strong repulsive forces at the beginning of the scan. Once the scan begins, the cantilever reaches a steady-state set-point, which is a DC value representing the desired oscillation amplitude of the cantilever.
During scanning, tip oscillation is obtained due to the tip-sample interaction by using a quadrant photodiode. Two bandpass filters with different center frequencies (first and third eigenmode resonance frequencies) are used: the first one filters the third eigenmode oscillation, which is used in the feedback loop. The filtered signal's envelope is measured by the amplitude detector to obtain comparable DC values. The detected amplitude is compared with the set point to generate an error signal. To minimize error signal saturation, a false error generator is used before the controller unit. The controller signal then adjusts the first eigenmode oscillation amplitude via a variable gain amplifier (VGA) in response to the generated error signal. The details of the amplitude detector (3.5) and false error generator (3.6) are explained next sections.

The second bandpass filter is used to filter the first eigenmode oscillation, which is phase-shifted by $180^{\circ}$ and multiplied by a gain, then added to the excitation signal, as explained in the *Q*-control section (3.2). This obtained oscillation is also used to obtain the surface topography of the sample. The oscillation envelope is detected and then inverted to reach the surface topography. The system schematic is illustrated in Figure 3.4.

### 3.4. System Parameters

The force required to excite a cantilever $F_D$ of a given free amplitude $A_0$ is given in equation 3.1.

$$F_D = kA_0/Q \tag{3.1}$$

Peak to peak first eigenmde free-air amplitude $A_{0,1} = 100$ nm and third eigenmode free-air amplitude $A_{0,3} = 1$ nm are selected. In Simulink, $F_D$ is employed to the system via peak-to-peak amplitude of a sine wave.

A bias is also implemented to sine wave for third eigenmode oscillation. The set-point values are chosen to be $A_{set}/A_0 = 90\%$ , $A_{set} = 0.9$ nm. System parameters are expressed in Table 3.1.

Table 3.1. System paramaters

| | |
|---|---|
| Hamaker Constant (*H*) | 10−19 J (in air) |
| | 10−20 J (in liquid) |
| Tip Radius (*R*) | 5 nm |
| Elasticity (*E*) | 100 GPa |
| *Qeff* | 3 (in air) |
| | 1.5 (in liquid) |

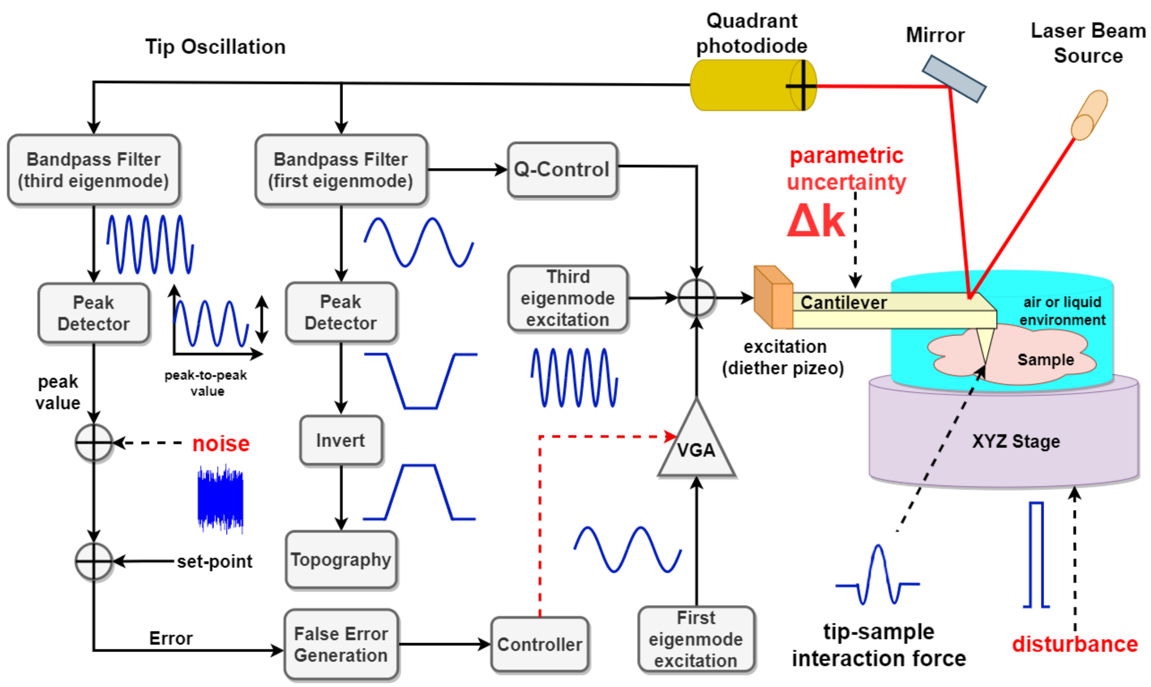


Figure 3.4. General structure of the HS-AFM model by using *Q*-controlled first eigenmode of the cantilever

Additionally, the performance of the controllers is assessed under both ideal conditions and the influence of exogenous factors such as noise, disturbance, and uncertainty for comparative purposes.

The chosen properties of the cantilevers which are the *Q*-factor, spring constant, and first three resonance frequencies of the cantilever are given in Table 3.2. The cantilever's first three flexural eigenmodes are implemented.

Table 3.2. Properties of the first three flexural eigenmodes of the cantilever

| Eigenmode n | Spring constant $k_n$ (N/m) | Quality factor $Q_n$ | Resonance Frequency $f_n$ (MHz) |
|---|---|---|---|
| High frequency cantilever (NanoWorld USC-F5-k30) in air | | | |
| 1 | 30 | 150 | 5 |
| 2 | 1190 | 300 | 31.5 |
| 3 | 9187 | 600 | 87.5 |
| High frequency cantilever (REF. [3]) in liquid | | | |
| 1 | 0.2 | 2 | 1.2 |
| 2 | 8 | 4 | 7.6 |
| 3 | 61 | 8 | 21 |

## 3.5. Amplitude Detector

An amplitude detector is designed to extract the envelope of the tip oscillation. In our setup, two amplitude detectors are used after a bandpass filter, as shown in Figure 3.4. The first detector, which is placed after the bandpass filter whose center frequency is the first eigenmode frequency, detects the amplitude change of the first eigenmode oscillation to obtain the topography of the sample. The second amplitude detector, which is placed after the bandpass filter whose center frequency is the third eigenmode frequency, detects the amplitude change of the third eigenmode oscillation and converts it to a DC value, which is then compared to a preset constant set-point.

In MATLAB/Simulink, the amplitude detector is designed with pulse generators, minimum-maximum function blocks, and switches as shown in Figure 3.5.

The min and max blocks find the minimum and maximum values of the given oscillation, triggered by pulse generators with a period equal to the oscillation period. To define the surface topography more accurately, a phase delay of 25% and 10% of the oscillation period is required for the upper and lower envelopes, respectively. Switches are also triggered by the pulse generators with a period equal to the oscillation period [57].

The peak-to-peak amplitude change is obtained by subtracting the lower envelope from the upper envelope. The lower envelope, upper envelope, and peak-to-peak amplitude change are shown in Figure 3.6.

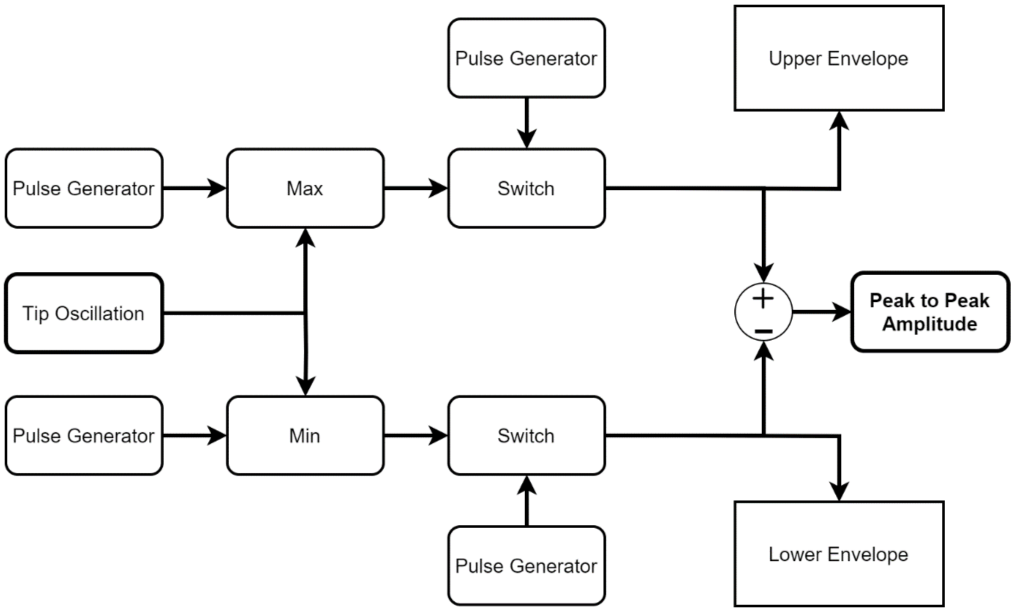


Figure 3.5. The block diagram of the amplitude detector

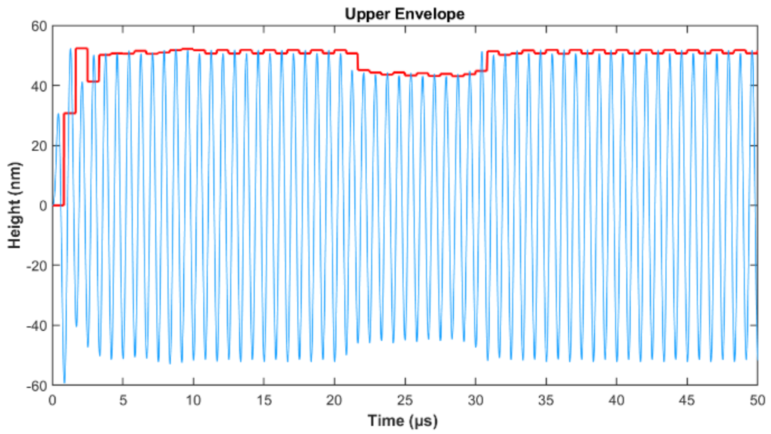


Figure 3.6. Upper envelope of the tip oscillation

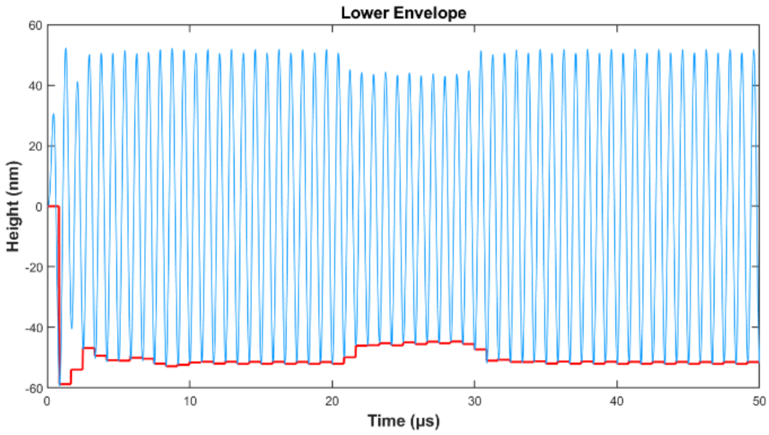


Figure 3.7. Lower envelope of the tip oscillation

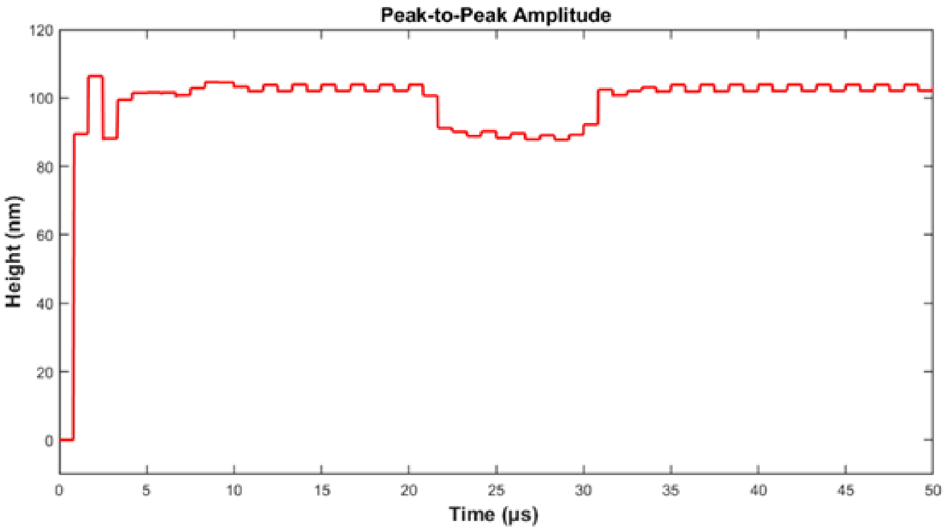


Figure 3.8. Peak detector output

### 3.6. False Error Generation

The error signal is the difference between the set point and the amplitude change detected by the amplitude detector. In state-of-the-art HS-AFM, the error signal is used to adjust the *z*-piezo's motion. However, in the system used in this thesis, the error signal is used to determine the cantilever excitation amplitude. By using the proposed method, the limitation of the *z*-piezo's motion is eliminated. However, the error signal limits are still valid due to the difference between the free-air amplitude and the set point. Especially when the sample has a rough surface topography, this limitation causes a slow feedback loop response, known as error signal saturation. To avoid error signal saturation also known as the parachuting effect, false error generator blocks are employed in the system feedback loop as shown in

Figure 3.4. After the error signal is generated, a false error generation block is added. The lower limit of the false error generator is set to a constant value. This threshold is adjusted due to the difference between the set point and free air amplitude [57-58]. When the error signal exceeds this threshold, the false error generator becomes active and produces a false error by multiplying it with a false error gain. This false error is then added to the actual error. The actual error and false error along with the topography are shown in Figure 3.7-a. The effect of false error generation is shown in Figure 3.7-b. As shown in Figure 3.7, the generated false error accelerates the controller response.

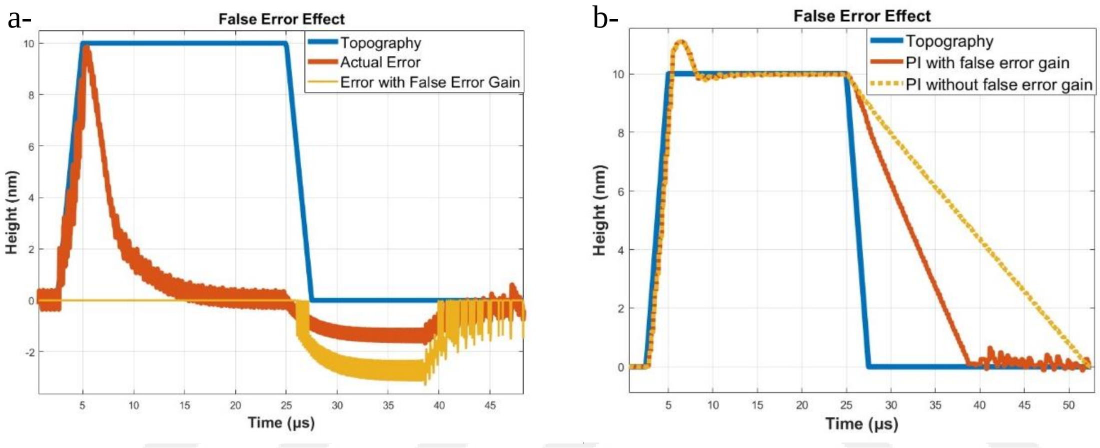


Figure 3.9. The effect of false error generation, a) Comparing false and actual errors, b) The response of the PI controller with and without false error

The false error gain is adjusted to ensure that the negative oscillation overshoot after a downward step in the topography does not exceed 10% of the height of the topography. Because the controller response to the upward step is sufficiently fast, there is no need to use an upper limit for the false error.

# 4. CONTROLLER DESIGN

After defining system parameters as given in section 3.4, it is necessary to optimize the controller for the feedback loop. Three different controllers are used in this system with the proposed method: the conventional PI controller, the robust $H_\infty$ controller, and the combination of $H_\infty$ and proportional control called $H_\infty$ + P. $H_\infty$ + P, which is used to combine the advantageous features of both the PI and $H_\infty$ controllers.

The controllers are tuned using an aggressive mode, which is a control strategy that prioritizes the speed of the feedback response over other factors while ensuring system stability. A false error generator is applied after optimizing controllers.

## 4.1. Why Feedback is Needed?

There are several types of feedback loops that can be used in an AFM system, depending on the operating mode being used. In contact mode AFM, the feedback is used to keep the distance constant between the cantilever tip and the sample. The height of the cantilever is adjusted by the feedback control loop, and the cantilever deflection remains constant. Without feedback, the cantilever is fixed at a constant height, and the deflection of the cantilever is measured. Finally, the topography image is obtained by measuring this deflection.

In dynamic mode AFM, the feedback loop is used to maintain constant oscillation amplitude to keep the height of the cantilever at a fixed point. This mode is especially used for fragile samples. The block diagram of the feedback loop is illustrated in Figure 4.1. Basically, tip oscillation is the cantilever response of the sample surface topography detected by a photodiode. A peak detector is used to detect peaks of the tip oscillation. The error signal is produced by subtracting oscillation peaks and set points. The controller adjusts the distance between the tip and sample by using a *z*-axis piezo actuator due to the error signal. The control signal is also used to generate an image.

Overall, in a conventional AFM system, feedback control is necessary to maintain the position of the cantilever tip on the sample surface and to ensure that the tip-sample interaction forces are within the desired range [59-60]. On the other hand, the system with the proposed method does not use a piezo to eliminate the limitations associated with it. As a result, the system transient response is faster.

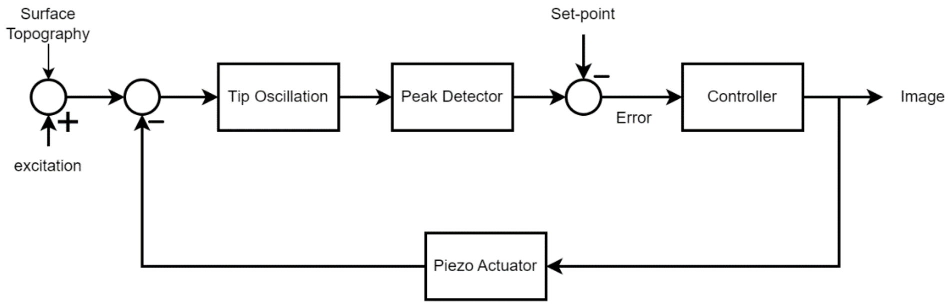


Figure 4.1. The block diagram of the dynamic mode AFM feedback loop

## 4.2. PI Control

PI is a commonly used controller in AFM systems because of its simplicity of integration into the system. They are widely used in many control applications, including AFM systems, because of their ability to provide stable and robust control over the system. Basically, a PI controller consists of a proportional gain Kp which provides a response proportional to the current error signal, and an integral gain Ki controller which provides a response based on the accumulated error over time. The feedback loop of the PI controller is given in Figure 4.2. The controller produces a control signal which adjusts the VGA to reach the set point. The control signal $u(t)$ is expressed in

$$u(t) = K_p e(t) + K_i \int e(t) \tag{4.1}$$

And the control signal in Laplace domain is

$$U(s) = G_1(s)E(s)\ where\ \ G_1(s) = \frac{K_p s + K_i}{s} \tag{4.2}$$

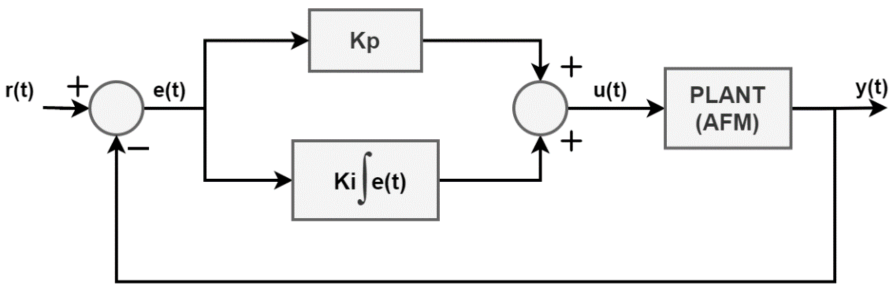


Figure 4.2. The closed loop block diagram of the PI controller

To adjust appropriate $K_p$ and $K_i$ values for the PI controller, the Ziegler-Nichols method is used as given in Table 4.1. $K_{cr}$ is the $K_p$ when the controller response oscillates at a period $T_{cr}$ as shown in Figure 4.3. This method is based on increasing the $K_p$ until it reaches $K_{cr}$ while $K_i$ is 0. After measuring $T_{cr}$ and $K_{cr}$, PI controller gains are adjusted by using Table 4.1.

Table 4.1. Ziegler-Nichols method

| Ziegler – Nichols Method | | | |
|---|---|---|---|
| Control Type | $K_p$ | $K_i$ | $K_D$ |
| PI | $0.45K_{cr}$ | $1.2K_p/T_{cr}$ | - |

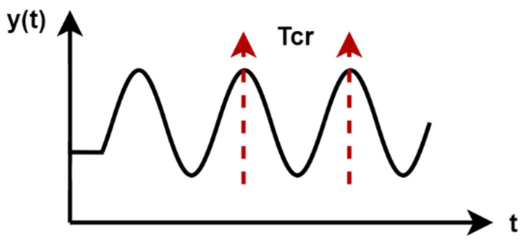


Figure 4.3. An oscillation with a period equal to the critical period

## 4.3. Closed Loop Transfer Function of the System

To define the closed loop transfer function of the system, the transfer function of the AFM plant is needed to define.

$C_i$ is defined as the transfer function of the i'th eigenmode of the cantilever and expressed as

$$C_i(s) = \frac{\frac{\omega_i^2}{k_i}}{s^2 + \frac{\omega_i}{Q_i}s + \omega_i^2} \quad (4.3)$$

The closed-loop transfer function of the system is known as (4.4) and is illustrated in Figure 4.4.

$$\frac{Y(s)}{R(s)} = \frac{G(s)}{1 + G(s)H(s)} \; where\; G(s) = G_1 G_2 \quad (4.4)$$

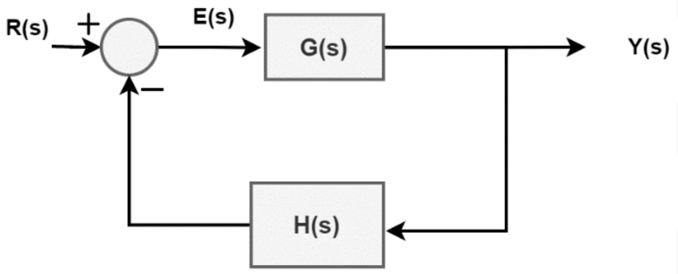


Figure 4.4. Transfer function of the closed loop system

Third eigenmode $C_3$ is used as a sensor while the *Q*-controlled cantilever as an actuator. The open loop transfer function of the system in the Laplace domain is defined as

$$G(s) = \alpha C_3 \frac{\sum_{k=1}^{3} C_i}{1 + \left(\frac{K_Q}{\omega_1}\sum_{k=1}^{3} C_i\right)s} \quad where\; K_Q = k\left(\frac{1}{Q_{eff}} - \frac{1}{Q}\right) \quad (4.5)$$

Here, H(s) = $\alpha C_3$, $\alpha$ is an interaction coefficient used to adjust the DC gain of the system. $K_Q$ is the *Q*-control gain. The *Q*-factor of the cantilever oscillation is effectively reduced to $Q_{eff}$ for each medium.

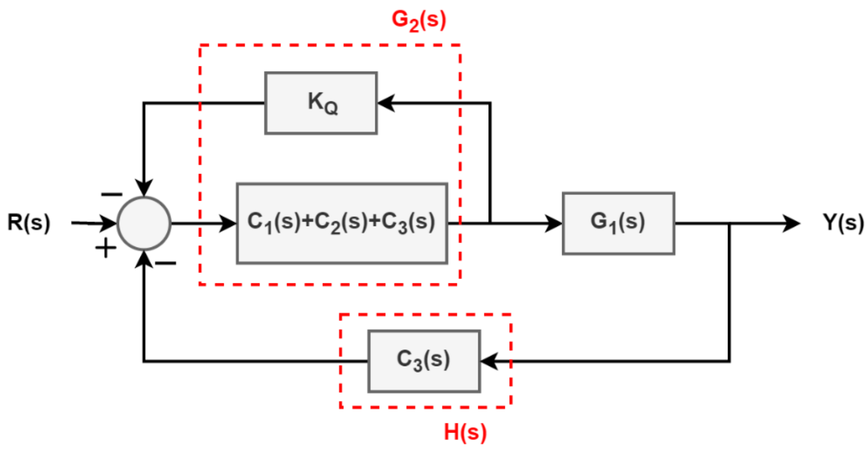


Figure 4.5. The closed loop block diagram of the system

## 4.4. Sensitivity and Complementary Sensitivity Functions

The main aim of designing a robust controller is good reference tracking, disturbance rejection, and noise attenuation.

The feedback closed loop of the system with reference *r*, error signal *e*, , control signal *u*, measured signal *y*, disturbance *d*, and measurement noise *n* is shown in Figure 4.6. Here, *K* is the robust controller and *G* is defined as a plant.

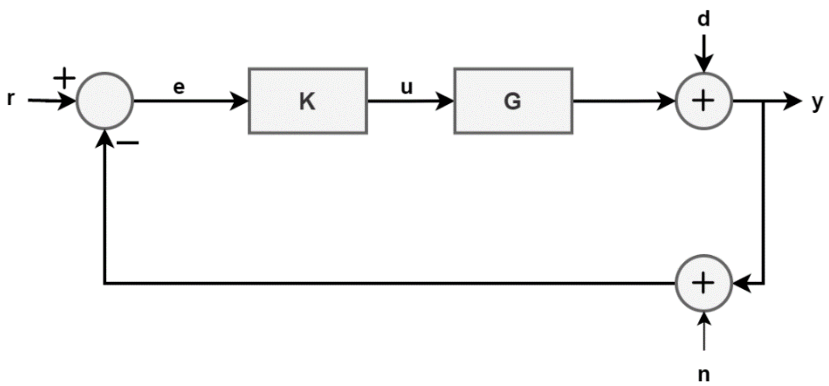


Figure 4.6. Block diagram of a basic feedback loop

Here, the error signal can be defined as

$$e = r - y - n \tag{4.6}$$

$$y = d + GK(r - y - n) \tag{4.7}$$

$$y = \underbrace{\frac{1}{1 + GK}}GK\,r + \underbrace{\frac{1}{1 + GK}}d - \underbrace{\frac{1}{1 + GK}}GK\,n \tag{4.8}$$

$$e = Sr - Sd + Tn \tag{4.9}$$

S is the sensitivity function that is the ratio of output to the disturbance of a system and T is the complementary sensitivity function which is the ratio of output to input of the system (S+T = 1). To achieve good reference tracking and disturbance rejection, it is important to minimize the error signal. This requires keeping the sensitivity function (S) low to attenuate disturbances and noise, especially at high frequencies.

Additionally, the complementary sensitivity function (T) should also be low to effectively reject noise at high frequencies. Since most of the noise is present at high frequencies, it is crucial to ensure that T is low in that range.

Therefore, in Figure 4.7, the plot should demonstrate a low sensitivity function at low frequencies and a low complementary sensitivity function at high frequencies, indicating effective noise attenuation and disturbance rejection.

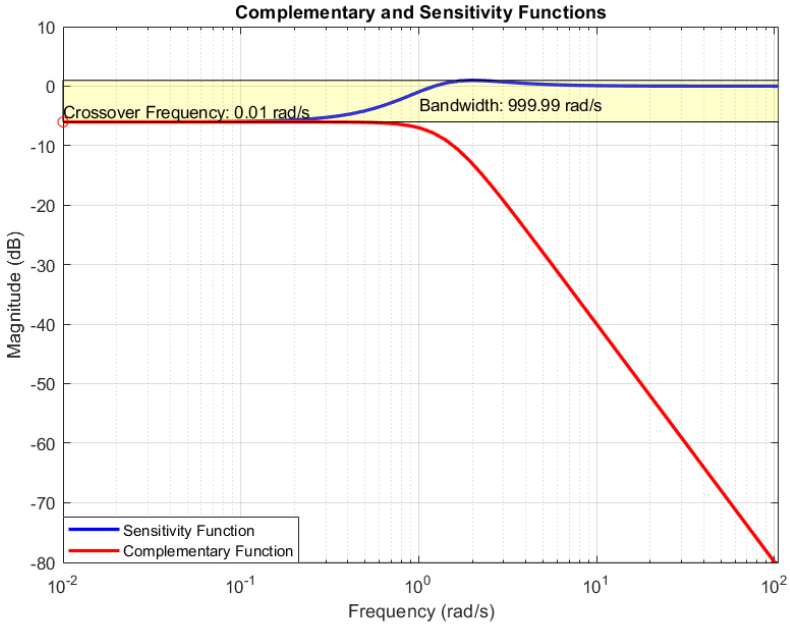


Figure 4.7. Bode Plot of Sensitivity and Complementary Sensitivity Functions

Here $\omega_{cr}$ is the cross-over frequency where sensitivity begins to get large and complementary begins to get small. The controller can be designed by adjusting the $\omega_{cr}$. By doing that, where the beginning of the noise attenuation and where the disturbance is dominant is determined in the frequency domain.

### 4.5. Robust H∞ Controller

H∞ controller is a robust controller designed to provide a reliable system to uncertainty, noise, and disturbance conditions. First of all, a robust controller problem must be defined as depicted in Figure 4.8. As mentioned before, *G* is the generalized plant which is the system to be controlled, *K* is the robust controller, ‘*w*’ is the vector of all exogenous inputs, ‘*z*’ is the vector of all errors, ‘*v*’ is the vector of the measurement variables and ‘*u*’ is the vector of all control variables. Here, *G* is represented as a transfer function matrix, taking into account multiple inputs and outputs. To shape the controller's robustness and performance more efficiently way, weight functions are defined for the system. Basically, by assigning different weights to different frequencies, the characteristics of the controller can be changed due to the system requirements.

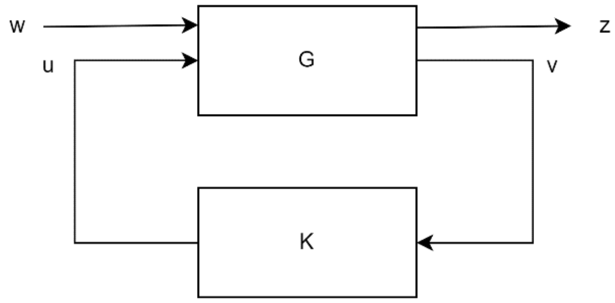


Figure 4.8. Robust control problem

The sensitivity weight function ($W_S$), complementary sensitivity weight function ($W_T$), and control weight function ($W_{KS}$) are shown in Figure 4.9. Here, $z_1$, $z_2$, and $z_3$ are the modified versions of *e*, *u*, and *y* by applying weight functions, respectively.

The generalized plant *P*, expressed below, includes both the original plant dynamics (*G*) and the weighting functions used in the H∞ control design [61].

$$P = \begin{bmatrix} A & B_1 & B_2 \\ C_1 & D_{11} & D_{12} \\ C_2 & D_{21} & D_{22} \end{bmatrix} \tag{4.10}$$

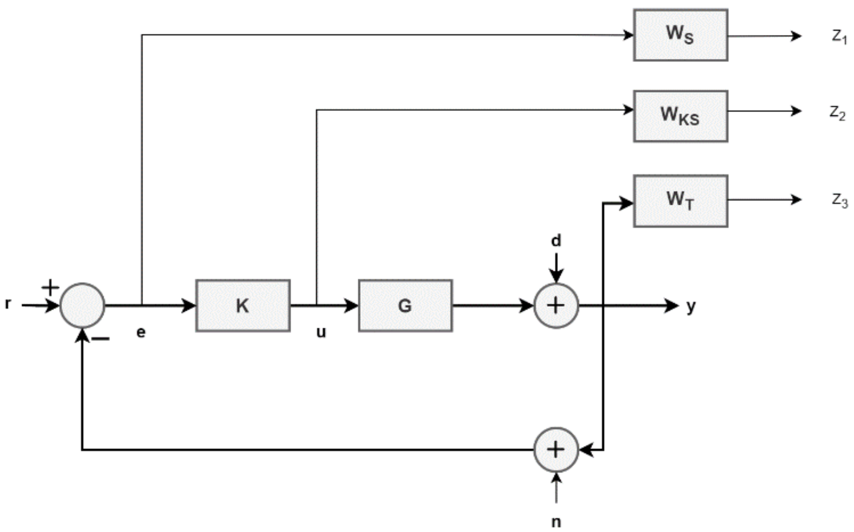


Figure 4.9. Weight functions for H∞ controller synthesis

The state matrix *A* represents the dynamics of the original plant *G*, the input matrix $B_1$ represents the inputs directly applied to the plant, and the input matrix $B_2$ represents the inputs that affect the plant through feedback.

The output matrix $C_1$ represents the outputs of the plant that are measured or controlled, the output matrix $C_2$ represents the outputs of the plant used for feedback control, the feedforward matrix $D_{11}$ represents the direct feedthrough from the inputs to the measured or controlled outputs, the feedforward matrix $D_{12}$ represents the feedthrough from the inputs to the outputs used for feedback control, the feedback matrix $D_{21}$ represents the feedthrough from the outputs used for feedback control to the measured or controlled outputs and the feedback matrix $D_{22}$ represents the internal feedback loop within the plant.

When designing an $H_\infty$ controller, a trade-off needs to be made between disturbance rejection and reference tracking to meet the system requirements. This situation is known as the mixed sensitivity problem. Mathematically, the mixed sensitivity problem can be formulated as follows

$$\|T_{zw}\|_\infty = \left\| \begin{matrix} W_S S \\ W_{KS} KS \\ W_T T \end{matrix} \right\|_\infty \leq \gamma \tag{4.11}$$

$\|T_{zw}\|_\infty$ represents the $H_\infty$ norm of the transfer function from the input *w* to the output *z* in the augmented plant *G*.

γ is the specified upper bound on the maximum sensitivity function gain, which determines the desired trade-off between performance and robustness. $H_\infty$ optimal controller *K* is found to minimize γ which is desired to be less than or equal to 1.

In this study, only the output sensitivity and complementary sensitivity are weighted depending on system requirements. The level of the input disturbance rejection is analyzed due to the frequency characteristics of the controller sensitivity *KS* in high frequencies. In this study, the defined weights for sensitivity ($W_S$) and complementary sensitivity ($W_T$), and control weight function ($W_{KS}$) are as expressed as follows

$$W_S = \frac{\frac{s}{M_S} + \omega_b}{s + \omega_b \epsilon} \qquad S \leq 1/W_S \tag{4.12}$$

$$W_T = 1 \qquad T \leq 1/W_T \tag{4.13}$$

$$W_{KS} = \frac{\alpha}{k_1 k_3} \tag{4.14}$$

$M_S$ refers to the magnitude of sensitivity peak in the frequency domain and is chosen as 2. $\omega_b$ represents the desired bandwidth for the sensitivity function. $\epsilon$ is the maximum gain of the $1/W_S$, which is also expressed as the desired steady-state error. For good reference tracking performance, $\epsilon$ is selected as 0.001. However, it cannot be decreased further to ensure good disturbance rejection, as this is limited by the mixed sensitivity problem.

The $H_\infty$ controller synthesis is tuned by increasing the $\omega_b$, which expands the bandwidth of the system, and decreasing α in the open-loop transfer function, thereby increasing the DC gain of the system, while ensuring system stability.

$H_\infty$ norm is often calculated using numerical techniques such as linear matrix inequalities (LMIs) or convex optimization algorithms. In this study, $H_\infty$ controller synthesis is done by using Control System Toolbox and Robust Control Toolbox provided by MATLAB. Designed controller parameters for both medium and controller can be found in Table 4.2.

Table 4.2. Design parameters of the controllers

| Medium | PI Controller | | | $H_\infty$ Controller | | | $H_\infty$+P Controller | | | |
|---|---|---|---|---|---|---|---|---|---|---|
| | P Gain | I Gain (x $10^6$) | False Error Gain | $\alpha$ | $\omega_b$ (krad/s) | False Error Gain | $\alpha$ | $\omega_b$ (rad/s) | P Gain | False Error Gain |
| Air | 27 | 8.8 | 2 | 500 | 0.7 | 11 | 500 | 1400 | 15.8 | 4 |
| Liquid | 9 | 3.3 | 2 | 20 | 1000 | 3 | **NA** | **NA** | **NA** | **NA** |

# 5. RESULTS AND DISCUSSION

In order to evaluate and compare various controller approaches, a topography is defined in the MATLAB environment. A single sample feature is defined as a pulse starting from 0 nm, with a height of 10 nm. The rising and falling edges are considered ramps, with a width equal to 10% of the total pulse width. The total topography in a frame is represented by 10 identical sample features on the *x*-axis and 100 identical sample features on the *y*-axis, as illustrated in Figure 5.1.

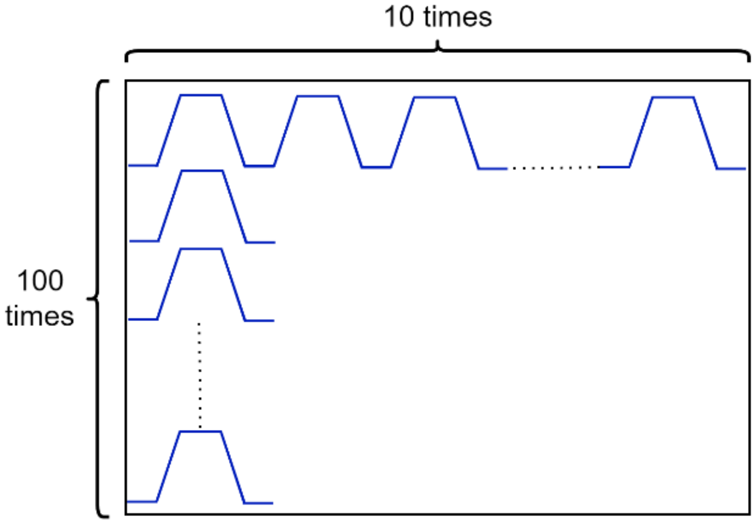


Figure 5.1. The overall topography in a frame

The simulation is performed in ideal conditions for both air and liquid mediums, utilizing a high-frequency cantilever. Furthermore, the performance of the controller is assessed in terms of scan rate and accuracy, considering noise, disturbances, and uncertainties for the same topography.

## 5.1. Acquisition Time

The scan rate represents the acquisition time required to scan a sample feature. By determining the acquisition time required for capturing a single sample feature, it becomes possible to assess the frame rate necessary to obtain a complete topography of the sample.

## 5.2. Acquisition Error

Acquisition error is the error between topography and first eigenmode oscillation amplitude expressed as an equation [57].

$$\text{Acquisition Error} = \frac{\int|\text{first eigenmode amplitude} - \text{topography}|}{\int|\text{topography}|} \text{ x } 100\% \qquad (5.1)$$

## 5.3. Exogenous Effects

Exogenous effects refer to external factors that affect the system but are not directly influenced by the system itself. These effects are typically considered as inputs to the system and are treated as independent variables. In this study, noise, disturbances, and uncertainties are applied to the system model individually. The robustness of the control approaches is compared based on their responses to exogenous effects.

## 5.4. Disturbance Rejection

Disturbance rejection refers to the ability of a controller to minimize the effects of disturbances on a system's performance. A controller with good disturbance rejection is capable of effectively compensating for disturbances, ensuring that the system remains stable and operates as desired. To test the disturbance rejection of the controllers, a pulse with a height of 100 nm is defined and employed as the topography of the system.

## 5.5. Noise Attenuation

Noise attenuation of a controller refers to the ability of the controller to suppress the effects of noise on the system's performance. A controller with effective noise attenuation capabilities can minimize the impact of noise, ensuring that it does not significantly degrade the desired system behavior. To test the noise attenuation of the controller, a Gaussian white noise with an RMS value of 1 Angstrom (Figure 5.2) is added after filtering the third eigenmode oscillation.

## 5.6. Uncertainty

Parametric uncertainty refers to the uncertainty or variability in the values of the system parameters. In this study, uncertainty is introduced by considering variations in the spring constant of the cantilever. The controllers' responses are evaluated by modifying the spring constant by 50% from its nominal value. PI, $H_\infty$, and $H_\infty$ + P controllers are used in this simulation.

The $H_\infty$ + P controller is essentially obtained by adding a proportional gain to the $H_\infty$ controller, aiming for a faster response based on the robust controller.

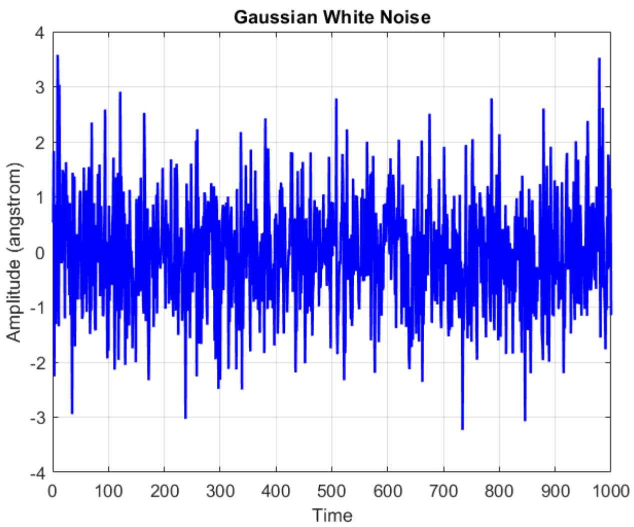


Figure 5.2. Gaussian white noise

The $H_\infty$ + P method is only employed in an air environment since both the PI and $H_\infty$ controllers yield nearly identical responses in terms of their fundamental eigenmode amplitudes, which is a characteristic of the method itself. The controllers are fine-tuned such that overshoot does not exceed 10% of the topography height. Due to variations in acquisition time, each controller exhibits a different pulse duration. Therefore, when selecting the pulse duration for a sample topography, it is based on the slower controller. Specifically, the chosen duration corresponds to the time at which the response of the slower controller reaches 99% of the topography's height before the falling edge. All controller parameters are given in Table 5.1.

Table 5.1. Acquisition time and error of all controllers

| Medium | Min. Acquisition time[1] for PI control ($\mu$s) | Frame rate[2] (fps) for PI control | Error in acquired topography[3] (%) | | | Min. Acquisition time[4] for $H_\infty$ control ($\mu$s) | Frame rate[5] (fps) for $H_\infty$ control | Min. Acquisition time[6] for $H_\infty$+P control ($\mu$s) | Frame rate[7] (fps) for $H_\infty$+P control |
|---|---|---|---|---|---|---|---|---|---|
| | | | PI | $H_\infty$ | $H_\infty$+ P | | | | |
| Air | 50 | 20 | 29 | 42 | 35 | 84 | 12 | 58 | 17 |
| Liquid | 20 | 50 | 36.7 | 36.8 | **NA** | 20 | 50 | **NA** | **NA** |

[1] Acquisition time of the feature

[2] In the frame, 10 identical features like the ones seen in Figure 5.1 on the fast scan axis, and 100 scan lines in the slow scan axis are assumed.

[3] Calculated from the acquisition error formula in [46]

[4, 6] Obtained for the same percentage error of PI controller.

[5] Obtained from the min. acquisition time found for $H_\infty$ controller.

[7] Obtained from the min. acquisition time found for $H_\infty$+P controller.

## 5.7. High Frequency Cantilever in Air

Figure 5.3 illustrates the frequency responses of the closed-loop sensitivity functions. It can be observed from Figure 5.3-a and Figure 5.3-b that the magnitude of the sensitivity and complementary sensitivity functions (S) for all controllers remains below the threshold (1/W). Among the controllers, the PI controller exhibits a slightly higher bandwidth compared to the others. In the low-frequency range, the sensitivity function and the sensitivity & plant function (Figure 5.3-c) with the PI controller exhibit lower gains than the other controllers. This is due to the presence of integral gain. Theoretically, this characteristic leads to a lower steady-state error and improved performance in rejecting disturbances. It is important to note that while sensitivity functions provide insights into the time-domain performance, simulation results may deviate from expectations due to false error gains. As shown in Figure 5.3-d, in high frequencies, the $H_\infty$ controller has less gain than the other controllers. This means that the PI and $H_\infty$+P controllers can be corrupted under noisy conditions. According to Figure 5.4-a, the PI controller exhibits significantly higher DC gain than the other controllers in low frequencies. Furthermore, in high frequencies, both the PI controller and the $H_\infty$+P controller demonstrate higher gain compared to the $H_\infty$ controller.

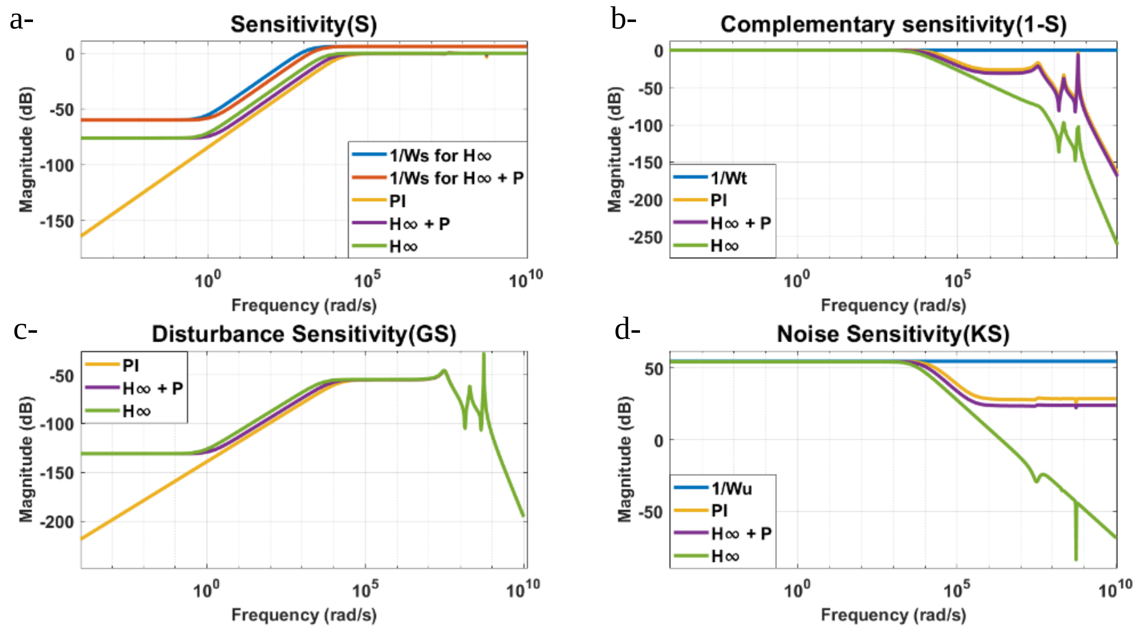


Figure 5.3. Magnitudes of the a) Sensitivity, b) Complementary sensitivity, c) Disturbance sensitivity, and d) Noise sensitivity functions for all controllers

In low frequencies, the PI controller has 90˚ phase lag with the error signal as shown in Figure 5.4-b. In high frequencies, PI and $H_\infty$+P are in phase with the error signal.

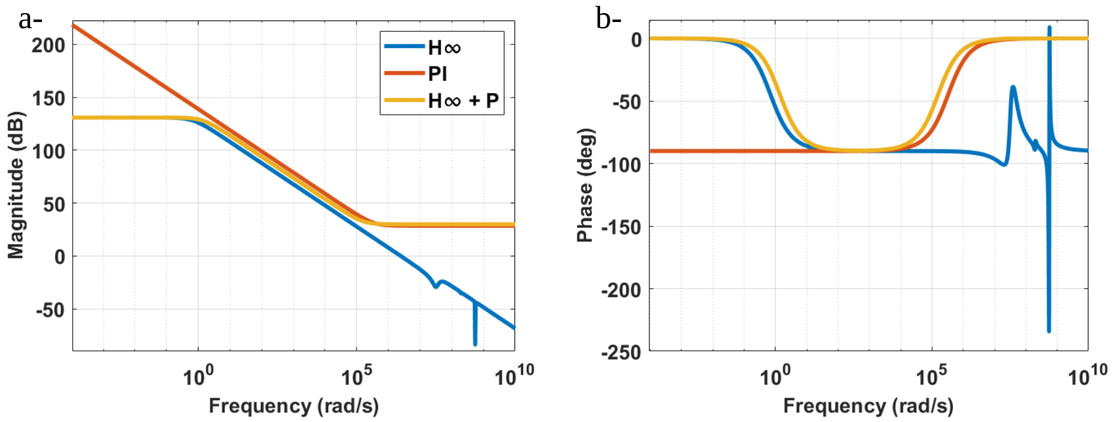


Figure 5.4. Bode plots of the controller’s transfer function, a) Magnitude response b) Phase response

The inverse of the fundamental eigenmode oscillation amplitude in air medium is the obtained topography in ideal conditions as shown in Figure 5.5. As expected from both sensitivity and controller response, the PI controller exhibits the fastest response. Moreover, all controller’s responses and obtained topography from the fundamental eigenmode amplitude under exogenous effects are shown in Figure 5.6.

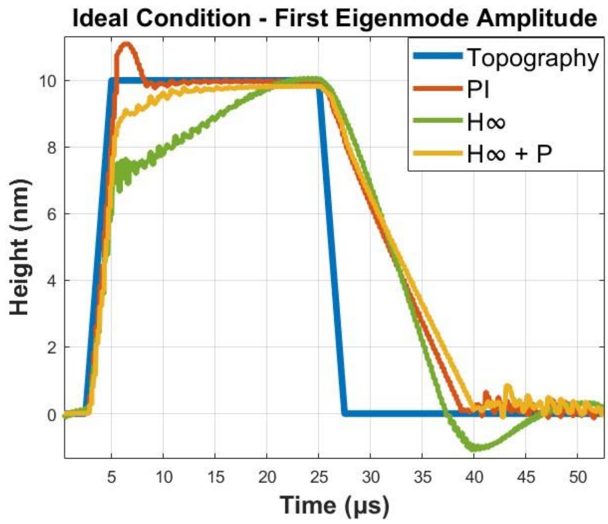


Figure 5.5. Obtained topography from all controllers

As seen in Figure 5.6-b, the PI response is corrupted under the effect of noise because of the high proportional gain. Conversely, $H_\infty$+P performs better under noisy conditions. In Figure 5.6-c, $H_\infty$ yields the worst response under the uncertainty condition, whereas the $H_\infty$+P controller exhibits the most robust response.

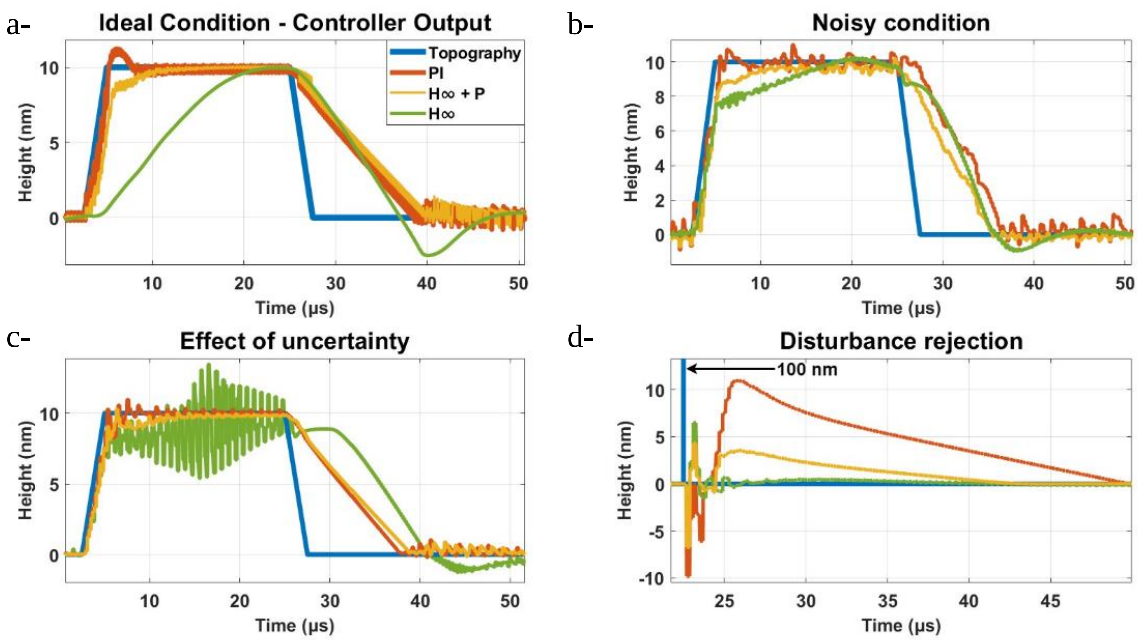


Figure 5.6. a) Controller response under ideal conditions, b) Obtained topography with noise, c) Uncertainty effect, and d) Disturbance effect

Figure 5.6-d illustrates that $H_\infty$ gives the most robust response to disturbance, while $H_\infty$+P provides better performance than PI.

Overall, H∞+P exhibits more preferable performance compared to the other controllers.

## 5.8. High Frequency Cantilever in Liquid

In a liquid environment, the H∞+P controller approach is not applied due to the close response of the topography obtained from the first eigenmode oscillation amplitude (Figure 5.8-a). This is due to the method of using the *Q*-controlled fundamental eigenmode as an actuator in this system. Here, the PI controller has a slightly higher closed-loop bandwidth according to Figure 5.7-a. PI controller exceeds the limits provided by the complementary sensitivity function, as depicted in Figure 5.7-b.

This can lead the instability under parametric uncertainty. As observed in the context of the air medium, the PI controller exhibits lower gain due to the integral component (Figure 5.7-c). Since the PI controller exceeds the threshold (1/Wu), it can yield an inferior response in the presence of noise.

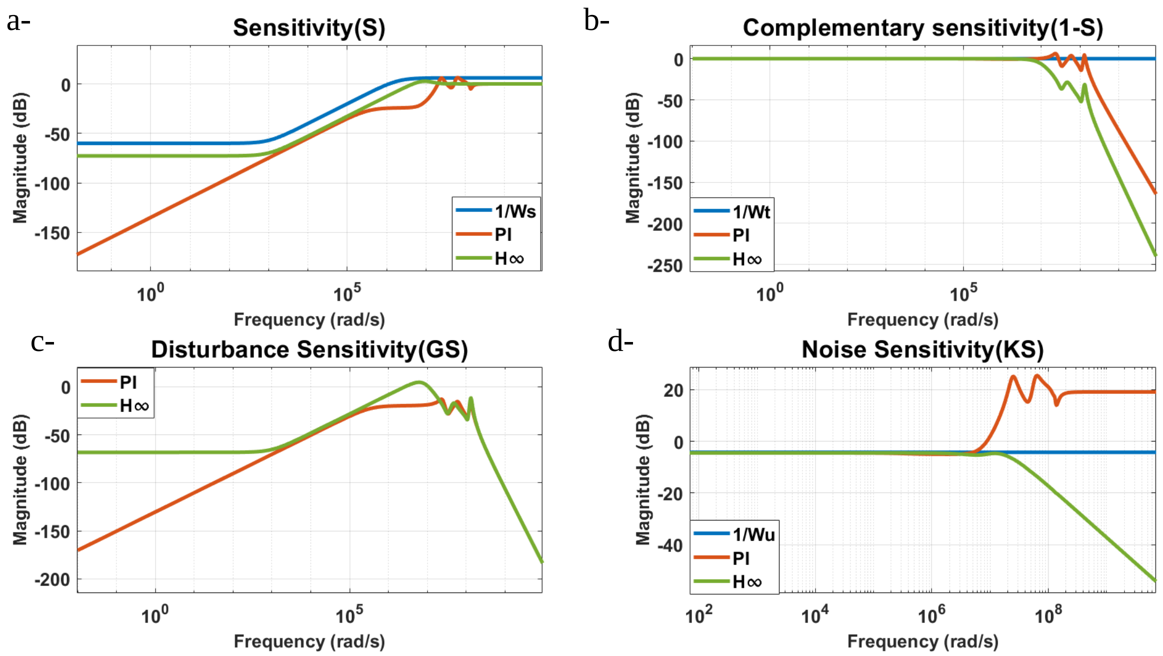


Figure 5.7. Magnitudes of the a) Sensitivity, b) Complementary sensitivity, c) Disturbance sensitivity, and d) Noise sensitivity functions for all controllers

In Figure 5.8-c, under parametric uncertainty conditions, the PI controller is slightly more affected than the H∞ controller as expected from the complementary sensitivity function. Both controllers exhibit the same response to the disturbance.

Even with the bad response of the controllers (Figure 5.9-a), fundamental eigenmode oscillation gives a very close response to the original topography (Figure 5.8-a).

The obtained topography from the first eigenmode amplitude under noise is shown in Figure 5.8-b. Here, the effect of the exceeding noise sensitivity plot for the PI controller is not seen in the obtained topography. However, As expected from the noise sensitivity plot, the PI controller response is corrupted under noisy conditions as seen in Figure 5.9-b. This case shows that the usage of the first eigenmode amplitude as an actuator eliminates the high-frequency noise.

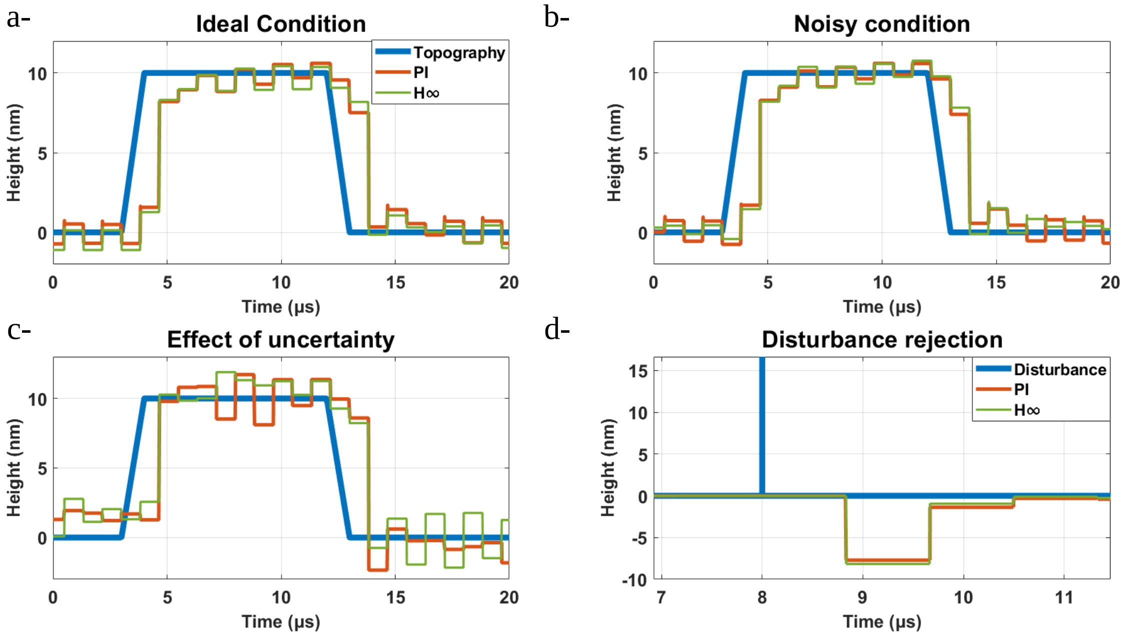


Figure 5.8. a) Obtained topography under ideal conditions, b) Obtained topography under noise, c) Uncertainty effect on topography, and d) Disturbance effect on topography

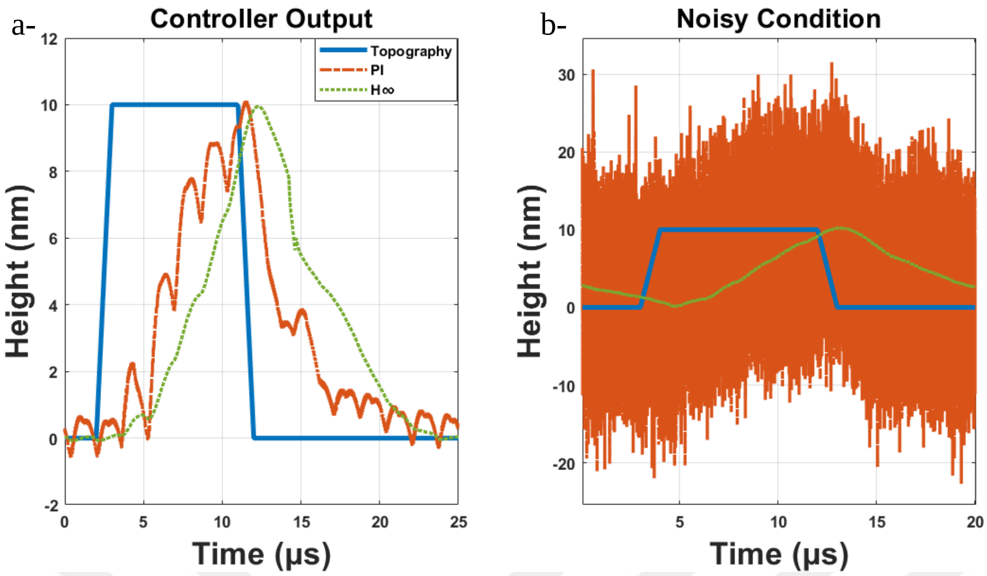


Figure 5.9. a) Output of PI and $H_\infty$ controllers under ideal conditions, and b) Output of PI and $H_\infty$ controllers under noisy conditions

# 6. CONCLUSION AND OUTLOOK

In this study, a dynamic HS-AFM system with a *Q*-controlled cantilever is simulated using different controllers: PI, $H_\infty$, and $H_\infty$+ P, within the MATLAB/Simulink environment. All controllers are compared based on acquisition error, frame rate, and their performance under exogenous effects for both environments. The results indicate that there is no significant difference in performance between the PI and $H_\infty$ controllers in a liquid medium because of the using method. Therefore, the $H_\infty$+ P controller, which combines the advantages of both controllers, is proposed only for the air environment. However, in the air environment, the PI controller demonstrates a faster operating speed compared to the $H_\infty$ controllers, contrary to what is commonly reported in the literature under ideal conditions.

Furthermore, the $H_\infty$+ P controller exhibits superior overall performance compared to the others under exogenous effects. The proposed HS-AFM system achieves image acquisition in 50 milliseconds per frame in a liquid medium and 20 milliseconds per frame in an air environment, representing a significantly higher scan speed than the current state-of-the-art HS-AFM systems [62].

This study utilized an HS-AFM system, where a pulse with a rectangular shape is employed as the topography. To enhance the evaluation of system response in future studies, it is recommended to utilize actual AFM images as topographical inputs. This approach allows testing the system's performance on various types of samples. Furthermore, adjusting system parameters based on sample elasticity due to the sample can be beneficial. For instance, when dealing with softer samples, reducing Young's modulus or modifying cantilever parameters can be considered. Moreover, the HS-AFM system can be enhanced through the implementation of different controller approaches, such as adaptive control, repetitive control, model predictive control, and neural network-based control. To expand the capabilities of the proposed HS-AFM system, it is advisable to integrate it into an embedded system, such as an FPGA or a microprocessor.

## REFERENCES


1. Xia, F., and Youcef-Toumi, K.. (2022). Review: Advanced Atomic Force Microscopy Modes for Biomedical Research. *Biosensors*, 12(12), 1116.

2. Binnig, G., Quate, C. F., and Gerber, C.. (1986). Atomic Force Microscope. *Physical Review Letters*, 56(9), 930–933.

3. Ando, T.. (2012). High-speed atomic force microscopy coming of age. *Nanotechnology*, 23(6), 062001.

4. Ando, T., Uchihashi, T., and Kodera, N.. (2013). High-Speed AFM and Applications to Biomolecular Systems. *Annual Review of Biophysics*, 42(1), 393–414.

5. Ando, T., Kodera, N., Naito, Y., Kinoshita, T., Furuta, K. Y., and Toyoshima, Y. Y. (2003). A high-speed atomic force microscope for studying biological macromolecules in action. *ChemPhysChem*, 4(11), 1196-1202.

6. Ando, T. (2014). High-speed AFM imaging. *Current Opinion in Structural Biology*, 28, 63-68.

7. Frederix, P. L., Bosshart, P. D., and Engel, A. (2009). Atomic force microscopy of biological membranes. *Biophysical Journal*, 96(2), 329-338.

8. Humphris, A. D. L., Miles, M. J., and Hobbs, J. K. (2005). A mechanical microscope: High-speed atomic force microscopy. *Applied Physics Letters*, 86(3), 034106.

9. Ando, T. (2019). High-speed atomic force microscopy. *Current Opinion in Chemical Biology*, 51, 105-112.

10. Kodera, N., Yamamoto, D., Ishikawa, R., and Ando, T.. (2010). Video imaging of walking myosin V by high-speed atomic force microscopy. *Nature*, 468(7320), 72–76.

11. Zhou, X., and Zhuo, R. (2022). Stability and contrast in bimodal amplitude modulation atomic force microscopy for different mode combinations in ambient air. *AIP Advances*, 12(5), 055321.

12. Kort-Kamp, W. J., Murdick, R. A., Htoon, H., and Jones, A. C. (2022). Utilization of coupled eigenmodes in Akiyama atomic force microscopy probes for bimodal multifrequency sensing. *Nanotechnology*, 33(45), 455501.

13. Shaik, N. H., Reifenberger, R. G., and Raman, A. (2020). Nanomechanical mapping in air or vacuum using multi-harmonic signals in tapping mode atomic force microscopy. *Nanotechnology*, 31(45), 455502.

14. Ebeling, D., and Solares, S. D.. (2013). Bimodal atomic force microscopy driving the higher eigenmode in frequency-modulation mode: Implementation, advantages, disadvantages and comparison to the open-loop case. *Beilstein Journal of Nanotechnology*, 4, 198–207.

15. Sulchek, T., Hsieh, R., Adams, J. D., Yaralioglu, G. G., Minne, S. C., Quate, C. F., Cleveland, J. P., Atalar, A., and Adderton, D. M.. (2000). High-speed tapping mode imaging with active Q control for atomic force microscopy. *Applied Physics Letters*, 76(11), 1473–1475.

16. Antognozzi, M., Szczelkun, M. D., Humphris, A. D. L., and Miles, M. J.. (2003). Increasing shear force microscopy scanning rate using active quality-factor control. *Applied Physics Letters*, 82(17), 2761–2763.

17. Kodera, N., Yamashita, H., and Ando, T.. (2005). Active damping of the scanner for high-speed atomic force microscopy. *Review of Scientific Instruments*, 76(5), 053708.

18. Fairbairn, M. W., Muller, P., and Moheimani, S. O. R.. (2014). Sensorless Implementation of a PPF Controller for Active *Q* Control of an AFM Microcantilever. *IEEE Transactions on Control Systems Technology*, 22(6), 2118–2126.

19. Ruppert, M. G., and Moheimani, S. R. (2015). Multimode *Q* control in tapping-mode AFM: Enabling imaging on higher flexural eigenmodes. *IEEE Transactions on Control Systems Technology*, 24(4), 1149-1159.

20. Balantekin, M., Satır, S., Torello, D., and Değertekin, F. L.. (2014). High-speed tapping-mode atomic force microscopy using a Q-controlled regular cantilever acting as the actuator: Proof-of-principle experiments. *Review of Scientific Instruments*, 85(12), 123705.

21. Balantekin, M.. (2015). High-speed dynamic atomic force microscopy by using a Q-controlled cantilever eigenmode as an actuator. *Ultramicroscopy*, 149, 45–50.

22. Bozchalooi, I. S., and Youcef-Toumi, K. (2014). Multi-actuation and PI control: A simple recipe for high-speed and large-range atomic force microscopy. *Ultramicroscopy*, 146, 117-124.

23. Messineo, S., Ragazzon, M. R. P., Busnelli, F., and Gravdahl, J. T.. (2022). Analysis of PI-Control for Atomic Force Microscopy in Contact Mode. *IEEE Transactions on Control Systems Technology*, 30(4), 1681–1695.

24. Schitter, G., Astrom, K. J., DeMartini, B. E., Thurner, P. J., Turner, K. L., and Hansma, P. K. (2007). Design and modeling of a high-speed AFM-scanner. *IEEE Transactions on Control Systems Technology*, 15(5), 906-915.

25. Basso, M., Paoletti, P., Tiribilli, B., and Vassalli, M. (2010). AFM imaging via nonlinear control of self-driven cantilever oscillations. *IEEE Transactions on Nanotechnology*, 10(3), 560-565.

26. Chuang, N., Petersen, I. R., and Pota, H. R. (2013). Robust H∞ control in fast atomic force microscopy. *Asian Journal of Control*, 15(3), 872-887.

27. Lee, C., and Salapaka, S. M. (2015). Model based control of dynamic atomic force microscope. *Review of Scientific Instruments*, 86(4), 043703.

28. Nakakuki, T., Ogawa, M., and Ishii, C. (2012, October). Nonlinear robust stage control of atomic force microscope. *In 2012 IEEE International Conference on Control Applications,* 539-544.

29. Putman, C. A. J., De Grooth, B. G., Van Hulst, N. F., and Greve, J.. (1992). A detailed analysis of the optical beam deflection technique for use in atomic force microscopy. *Journal of Applied Physics*, 72(1), 6–12.

30. Viani, M. B., Schäffer, T. E., Paloczi, G. T., Pietrasanta, L. I., Smith, B. L., Thompson, J. B., ... and Hansma, P. K. (1999). Fast imaging and fast force spectroscopy of single biopolymers with a new atomic force microscope designed for small cantilevers. *Review of Scientific Instruments*, 70(11), 4300-4303.

31. Fukuda, S., and Ando, T. (2021). Faster high-speed atomic force microscopy for imaging of biomolecular processes. *Review of Scientific Instruments*, 92(3), 033705.

32. Schitter, G., Stark, R. W., and Stemmer, A. (2004). Fast contact-mode atomic force microscopy on biological specimen by model-based control. *Ultramicroscopy*, 100(3-4), 253-257.

33. Schitter, G., Menold, P., Knapp, H. F., Allgöwer, F., and Stemmer, A. (2001). High performance feedback for fast scanning atomic force microscopes. *Review of Scientific Instruments*, 72(8), 3320-3327.

34. Schitter, G., Allgöwer, F., and Stemmer, A. (2003). A new control strategy for high-speed atomic force microscopy. *Nanotechnology*, 15(1), 108.

35. Wang, Y., Hu, X., and Xu, L. (2016). An intelligent control scheme for precise tip-motion control in atomic force microscopy. *Scanning*, 38(2), 93-99.

36. Coraggio, M., Homer, M., Payton, O. D., and Di Bernardo, M.. (2018). Improved Control Strategies for Atomic Force Microscopes in Intermittent Contact Mode. *IEEE Transactions on Control Systems Technology*, 26(5), 1673–1684.

37. Braunsmann, C., and Schäffer, T. E. (2010). High-speed atomic force microscopy for large scan sizes using small cantilevers. *Nanotechnology*, 21(22), 225705.

38. Valotteau, C., Sumbul, F., and Rico, F.. (2019). High-speed force spectroscopy: microsecond force measurements using ultrashort cantilevers. *Biophysical Reviews*, 11(5), 689–699.

39. Walters, D. A., Cleveland, J. P., Thomson, N. H., Hansma, P. K., Wendman, M. A., Gurley, G., and Elings, V. (1996). Short cantilevers for atomic force microscopy. *Review of Scientific Instruments*, 67(10), 3583-3590.

40. Brand, U., Xu, M., Doering, L., Langfahl-Klabes, J., Behle, H., Bütefisch, S., ... and Hauptmannl, M. (2020). Long Slender Piezo-Resistive Silicon Microprobes for Fast Measurements of Roughness and Mechanical Properties inside Micro-Holes with Diameters below 100 μm. *Sensors*, 19(6), 1410.

41. Uchihashi, T., Kodera, N., and Ando, T. (2012). Guide to video recording of structure dynamics and dynamic processes of proteins by high-speed atomic force microscopy. *Nature Protocols*, 7(6), 1193-1206.

42. Raman, A., Melcher, J., and Tung, R. (2008). Cantilever dynamics in atomic force microscopy. *Nano Today*, 3(1-2), 20-27.

43. Bozchalooi, I. S. (2015). *Design and control of high-speed and large-range atomic force microscope* (Doctoral dissertation, Massachusetts Institute of Technology, Department of Mechanical Engineering).

44. Ruppert, M. G., Harcombe, D. M., Ragazzon, M. R. P., Moheimani, S. O. R., and Fleming, A. J.. (2017). A review of demodulation techniques for amplitude-modulation atomic force microscopy. *Beilstein Journal of Nanotechnology*, 8, 1407–1426.

45. Rodrıguez, T. R., and García, R. (2002). Tip motion in amplitude modulation (tapping-mode) atomic-force microscopy: Comparison between continuous and point-mass models. *Applied Physics Letters*, 80(9), 1646-1648.

46. Severin, N., Dzhanoev, A. R., Lin, H., Rauf, A., Kirstein, S., Palma, C.-A., Sokolov, I. M., and Rabe, J. P.. (2022). Atomic resolution with high-eigenmode tapping mode atomic force microscopy. *Physical Review Research*, 4(2).

47. Fukuma, T., Yoshioka, S., and Asakawa, H.. (2011). Wideband phase-locked loop circuit with real-time phase correction for frequency modulation atomic force microscopy. *Review of Scientific Instruments*, 82(7), 073707.

48. Das, S. K., Badal, F. R., Rahman, M. A., Islam, M. A., Sarker, S. K., and Paul, N.. (2019). Improvement of Alternative Non-Raster Scanning Methods for High Speed Atomic Force Microscopy: A Review. *IEEE Access*, 7, 115603–115624.

49. Garcia, R., and Herruzo, E. T.. (2012). The emergence of multifrequency force microscopy. *Nature Nanotechnology*, 7(4), 217–226.

50. Santos, S., Lai, C. Y., Olukan, T., and Chiesa, M. (2017). Multifrequency AFM: from origins to convergence. *Nanoscale*, 9(16), 5038-5043.

51. Adams, J. D., Erickson, B. W., Grossenbacher, J., Brugger, J., Nievergelt, A., and Fantner, G. E.. (2016). Harnessing the damping properties of materials for high-speed atomic force microscopy. *Nature Nanotechnology*, 11(2), 147–151.

52. Hölscher, H., and Schwarz, U. D. (2007). Theory of amplitude modulation atomic force microscopy with and without Q-control. *International Journal of Non-linear Mechanics*, 42(4), 608-625.

53. Martin-Jimenez, D., Ihle, A., Ahles, S., Wegner, H. A., Schirmeisen, A., and Ebeling, D. (2020). Bond-level imaging of organic molecules using Q-controlled amplitude modulation atomic force microscopy. *Applied Physics Letters*, 117(13), 131601.

54. Coskun, M. B., Alemansour, H., Fowler, A. G., Maroufi, M., and Moheimani, S. O. R.. (2019). *Q* Control of an Active AFM Cantilever With Differential Sensing Configuration. *IEEE Transactions on Control Systems Technology*, 27(5), 2271–2278.

55. Sulchek, T., Hsieh, R., Adams, J. D., Yaralioglu, G. G., Minne, S. C., Quate, C. F., Cleveland, J. P., Atalar, A., and Adderton, D. M.. (2000). High-speed tapping mode imaging with active Q control for atomic force microscopy. *Applied Physics Letters*, 76(11), 1473–1475.

56. Tamayo, J., Humphris, A. D. L., Malloy, A. M., and Miles, M. J. (2001). Chemical sensors and biosensors in liquid environment based on microcantilevers with amplified quality factor. *Ultramicroscopy*, 86(1-2), 167-173.

57. Balantekin, M., and Değertekin, F. L.. (2011). Optimizing the driving scheme of a self-actuated atomic force microscope probe for high-speed applications. *Ultramicroscopy*, 111(8), 1388–1394.

58. Sulchek, T., Yaralioglu, G. G., Quate, C. F., and Minne, S. C. (2002). Characterization and optimization of scan speed for tapping-mode atomic force microscopy. *Review of Scientific Instruments*, 73(8), 2928-2936.

59. Orun, B., Necipoglu, S., Basdogan, C., and Guvenc, L.. (2009). State feedback control for adjusting the dynamic behavior of a piezoactuated bimorph atomic force microscopy probe. *Review of Scientific Instruments*, 80(6), 063701.

60. An, S.. (2022). Understanding the Feedback Circuit in an Atomic Force Microscope. *Applied Science and Convergence Technology*, 31(4), 99–102.

61. Bansal, A., and Sharma, V. (2013). Design and analysis of robust H-infinity controller. *Control Theory and Informatics*, 3(2), 7-14.

62. Coşar, A. (2018). *Nonlinear controller design for high speed dynamic atomic force microscope system* (Master Thesis, Izmir Institute of Technology (Turkey)).

*Gazili olmak ayrıcalıktır*